NanoTrends

Invites Research, Review and Popular Articles

NanoTrends attract scholarly contributions that fall under the broad tag of nanoscale science and technology. The coverage in general encompasses synthesis, characterization, studying properties, processing, fabrication and applications of the nanomaterials in the fields of electronics, medicine, healthcare, energy, biotechnology and environmental studies.

Over and above the articles of popular or general nature on the subject areas that fall under the scope of the NanoTrends are also considered for inclusion in the NanoTrends.

Features:

- Rapid online publication of papers, soon after their formal acceptance/ finalization.
- Promotional support to papers of specific interest on our web site www.nstc.in
- Online Submission of Manuscripts.
- Provides an online three tier stringent but smooth peer review process, with a highly acclaimed editorial board.
- Free online open access to the abstracts of all articles.
- Facilitates linking with the other authors or professionals.
- Worldwide circulation and visibility
- One year free access to authors whose papers are published in the NanoTrends (online).

Specific domains encompass:

Characterization techniques of Nanomaterials, Coupling of Properties at the Nanoscale, Films, Membranes, & Coatings, Nanoceramics, Metals & Alloys, Nanocomposites, Nanoparticles, Nanocrystals, Colloids, Sols, Nanoporous materials, Nanotubes, Nanowires, Nanofibers, Nanorods, & Nanobelts, Properties effected by Nanoscale Dimensions, Self-assemblies and directed assemblies etc.

Domains of Nanomaterials engineering & applications encompass:

Biomedical, Medicinal, Cosmetics & Drug development, Catalysis, Gas/Liquid Separations & Membrane reactors, Chemical, Petrochemical & Pharmaceutical, Conversion of Energy & Storage Devices/ Systems namely Fuel Cells & Solar Cells, Electrical, Electronics, Photonics & Magnetics, Telecommunications & Computational Studies, Food, Textile, Environmental, Construction, Transportation Nanomachines, Machine tools, Automobiles, Nanopatterning etc.

Above are the representatives lists of subject areas, NanoTrends in practice may accept other subject areas that fall under the defined broad scope and are consistence with the precise nano meter scale.

Information on every area of interests to the contributors is provided at one place under the head 'Authors' Corner'. One can reach to this corner by following the route, Publications-> NanoTrends Journal-> Authors' Corner in our website www.nstc.in. or clicking the link **http://www.nstc.in/journal/default.aspx**

Online manuscript submission may be done by following simple and self explanatory steps in the link **http://www.nstc.in/Journal/SubmitArticle.aspx,** Full manuscript must be sent to the NanoTrends through email **nanotrends@nstc.in**

Our contact details:

Publication Management Team 'NanoTrends'
Nano Science and Technology Consortium
A Division of Consortium e-Learning Network Pvt. Ltd.
A-118, 1st Floor, Sector-63, Noida, U.P., India, Pin-201301
Tel. : 0120- 4781207, 4781211, 4781215, 09810078958
E-mail: nanotrends@nstc.in Website: www.nstc.in

NSTC®
A Nanotechnology platform

NSTC is a division of Consortium E-learning Network and is India's premier organization working to promote the awareness of Nano-technology through advanced training and publications and commercialization of its application through our consultancy services. Statements and opinions expressed in the Journal reflect the views of the author(s) and are not the opinion of STM Journals unless so stated.

Subscription Information and Order:

Cost of Journal:

- National Subscription: Rs. 3750/- per Journal (includes 3 print issues), Single Issue copy purchase Rs.1500/copy
- International Subscription:
  - Online Only- $99, Print Only-$149 (includes 3 print issues)
  - Online + Print-$199 (includes 3 print issues + online access of published back volumes)

To purchase print compilation of back issues please send your query at **info@stmjournals.com, info@nstc.in**
Subscription must be prepaid. Rates outside the India includes speed delivery charges. Prices subject to change without notice.
Mode of Payment: At par cheque, Demand draft, and RTGS (payment to be made in favor of Consortium E-Learning Network. Pvt. ltd., payable at Delhi/New Delhi.

Online Access Policy

A). For Authors:
In order to provide maximum citation and wide publicity to the authors work, NanoTrends has an Open Access Policy, authors who would like to get their work open access can opt for Optional Open Access publication at nominal cost as follows

India, SARC and African Countries: INR 2500 or 100 USD including single hard copy of Author's Journal.

Other Countries: USD 200 including single hard copy of Author's Journal.

B.) For Subscribers:

- Online access will be activated within 72 hours of receipt of the payment (working days), subject to receipt of correct information on user details/Static IP address of the subscriber.
- The access will be blocked:
  - If the user requests for the same and furnishes valid reasons for blocking.
  - Due to technical issue.
  - Misuse of the access rights as per the access policy.

Advertising and Commercial Reprint Inquiries: NanoTrends with wide circulation and visibility offer an excellent media for showcasing/promotion of your products/services and the events-namely, Conferences, Symposia/Seminars etc. The journal has very high potential to deliver the message across the targeted audience regularly with each published issue. The advertisements on bulk subscriptions, gift subscriptions or reprint purchases for distribution etc. are also very welcome.

Lost Issue Claims: Please note the following when applying for lost or missing issues:

- Claims for print copies lost will be honored only after 45 days of the dispatch date and before publication of the next issue as per the frequency.
- Tracking id for the speed post will be provided to all our subscribers and the claims for the missing Journals will be entertained only with the proofs which will be verified at both the ends.
- Claims filed due to insufficient (or no notice) of change of address will not be honored.
- Change of Address of Dispatch should be intimated to STM Journals at least 2 months prior to the dispatch schedule as per the frequency by mentioning subscriber id and the subscription id.
- Refund requests will not be entertained.

Legal Disputes
All the legal disputes are subjected to Delhi Jurisdiction only.
If you have any questions, please contact the Publication Management Team:
info@stmjournals.com; Tel : +91 0120-4781211.

Publication Management Team (PMT)

NSTC's Academic Advisory Board

AAB

Editorial Board

eISSN 0973-418X

Nano Trends: A Journal of Nanotechnology and Its Applications
Volume 16, Issue 1, ISSN: 0973-418X

Effect of Disorder in Nanocrystalline $La_{0.5}Pr_{0.2}Ca_{1-x}Ba_xMnO_3$ Manganites

Nikesh A. Shah*
Department of Electronics, Saurashtra University, Rajkot-360005, India

Abstract

Nanocrystalline samples of $La_{0.5}Pr_{0.2}Ca_{0.3-x}Ba_xMnO_3$ (LPCBMO) (x = 0.05, 0.10, 0.15, 0.20, 0.25 and 0.30) manganites were successfully synthesized by employing prolonged grinding process in conventional solid-state reaction route. The obtained value of crystallite size (CS) varies from 76 nm in lower doped sample (x = 0.05) to 13 nm in the sample doped with Ba^{2+} (x) = 0.05. The variation in CS with x has been discussed in the context of larger the size mismatch at A-site cationic lattice, larger the structural disorder, higher the control over the crystallinity. The effect of crystallite size and other structural parameters on the transport properties of LPCBMO samples has been discussed in detail in the light of competition between the structural disorder effect and tolerance factor effect on the charge transport mechanism and proven that at nanoscale level also, the tolerance factor is effectively modifying the transport mechanism in manganites.

Keywords: *Nanocrystalline, manganites, tolerance factor*

****Author for Correspondence*** E-mail: snikesh@yahoo.com

INTRODUCTION

Giant magneto resistance (GMR) effect due to spin-dependent transport properties at the nanoscale non-magnetic insulating interface between two ferromagnetic thin layers has stimulated concentrated research in the field of nanoscience and nanotechnology. The phenomenon was first discovered in magnetic multilayers, such as Fe/Cr or Co/Cu [1] and later in heterogeneous magnetic alloys with ferromagnetic grains embodied in non-magnetic metallic or nonmetallic matrix [2, 3]. Magnetic and electric properties of granular transition metals and other ferromagnets have been known to depend on the grain size and inter-granular materials, which determine the inter-grain barriers [4]. Conductive electrons can drop from grain to grain through spin-dependent tunneling [5]. The probability of an electron tunneling across the inter-grain barrier is calculated considering an additional magnetic exchange energy arising when the magnetic moments of the neighboring grains are not parallel and assuming that the electron spin is conserved in tunneling. Randomly oriented spins of grains can be aligned under an external magnetic field. This gives rise to a significant increase in tunnel conductance, thereby reducing the resistivity of granular system.

Manganite perovskite has recently been studied extensively due to colossal magnetoresistance (CMR) mostly observed near the magnetic transition temperature (T_C). When the perovskite is in a ferromagnetic state, it behaves like a metal as to its electrical properties. In this sense, a granular perovskite is a conductive ferromagnet similar to a granular transition metal. However, the transport properties, especially the low-temperature transport properties, observed in granular perovskites with small grain size are obviously different from both in single crystal of manganite perovskite and in granular transition metals or in thin film. This suggests that the conductive origin of the granular perovskite also differs from these [6].

In GMR and CMR studies, grain morphology acts as an important tool to modify the materials properties, especially in crystalline manganites [7, 8]. In this article, we have studied the effect of nanocrystallite size and structural disorder on the transport properties of $La_{0.5}Pr_{0.2}Ca_{0.3-x}$ Ba_xMnO_3(LPCBMO)

(x = 0.05, 0.10, 0.15, 0.20, 0.25 and 0.30) manganites. Modifications in the transport behavior with crystallite size have been discussed in the context of crystalline boundaries and structural disorder induced by the chemical substitution.

EXPERIMENTAL DETAILS

Polycrystalline samples $La_{0.5}Pr_{0.2}Ca_{0.3-x}Ba_xMnO_3$(LPCBMO)(x = 0.05, 0.10, 0.15, 0.20, 0.25 and 0.30) system were synthesized using conventional solid-state reaction route with large time period of grinding to achieve the crystal size in nanoscale. Constituent oxides (La_2O_3, Pr_6O_{11} and MnO_2) and carbonates ($SrCO_3$ and $CaCO_3$) were mixed thoroughly in stoichiometric proportions and calcined at 950 °C for 24 h. These were ground (for long time duration ~ 12 h), pelletized and sintered in the temperature range of 1100–1300 °C for 24 h with many intermediate grindings. X-ray diffraction (XRD) patterns were recorded in the 2θ range of 20–80^o on a Siemens diffractometer. The resistivity measurements were carried using d.c. four-probe method on a physical property measurement system (PPMS, Quantum Design).

RESULTS AND DISCUSSION

Figure 1 shows the XRD patterns of all the LPCBMO samples understudy. They were indexed as single-phase compounds crystallizing in a distorted orthorhombic structure. Figure 2 shows a typical Rietveld refined XRD pattern of $LPCB_{0.20}MO$(x = 0.20) compound reveal the single-phasic nature of all the compounds having no detectable impurities. It is seen that there is an excellent agreement between experimental and Rietveld fitted patterns of $LPCB_{0.20}MO$ sample. Table 1 lists the values of Rietveld refined lattice parameters and unit cell volume for all the samples studied. It is clearly seen that with increase in x, the unit cell volume increases which can be ascribed to the larger-sized ion (Ba^{2+}: 0.147 nm) substation at smaller ionic site (Ca2+: 0.118 nm). Substitution of larger Ba ion at smaller Ca site results into the variation in size disorder which is increased from x = 0.05 to x = 0.30 (Table 2). Figure 3 shows an enlarged view of most intense XRD peaks of XRD patterns of all the samples revealing that with increase in x, the most intense peak shifts towards lower angle indicates the increase in lattice parameters and unit cell volume, as confirmed in Rietveld analysis of the XRD pattern. This indicates the high quality of the samples under study.

Table 1: *Values of Lattice Parameters and Unit Cell Volume for $La_{0.5}Pr_{0.2}Ca_{0.3-x}Ba_xMnO_3$ (LPCBMO) (x = 0.05, 0.10, 0.15, 0.20, 0.25 and 0.30) Manganites.*

$La_{0.5}Pr_{0.2}Ca_{0.3-x}Ba_xMnO_3$	a (nm)	b (nm)	c (nm)	V (nm^3)
x = 0.05	0.5466 (4)	0.7729 (2)	0.5472 (3)	0.23117
x = 0.10	0.5471 (1)	0.7731 (5)	0.5495 (6)	0.23242
x = 0.15	0.5479 (9)	0.7742 (8)	0.5512 (3)	0.23381
x = 0.20	0.5499 (6)	0.7769 (8)	0.5589 (4)	0.23877
x = 0.25	0.5512 (1)	0.7791 (2)	0.5648 (5)	0.24255
x = 0.30	0.5587 (5)	0.7816 (3)	0. 5704 (6)	0.24908

Table 2: *Values of Average A-Site Ionic Radius ($<r_A>$), A-Site Size Disorder (σ_A^2), Tolerance Factor (t), Peak Resistance and Peak Resistance Temperature for $La_{0.5}Pr_{0.2}Ca_{0.3-x}Ba_xMnO_3$ (LPCBMO) (x = 0.05, 0.10, 0.15, 0.20, 0.25 and 0.30) Manganites*

{σ^2 (r_A or r_B) = $<r^2_{A/B}> - <r_{A/B}>^2 = \Sigma x_i r_i^2 - (\Sigma x_i r_i)^2$ and $t = (r_A + r_O)/[\sqrt{2} \times (r_B + r_O)]$ [9]}.

$La_{0.5}Pr_{0.2}Ca_{0.3-x}Ba_xMnO_3$	$< r_A >$ (nm)	σ_{A2} (nm^2)($\times 10^{-5}$)	t	R_P (Ω)	T_{RP} (K)
x = 0.05	0.1212	3.81	0.9166	24098	147
x = 0.10	0.1227	6.87	0.9218	18410	151
x = 0.15	0.1241	9.51	0.9267	01174	165
x = 0.20	0.1256	11.7	0.9319	--	--
x = 0.25	0.1270	13.5	0.9368	00327	175
x = 0.30	0.1285	14.9	0.9420	00194	177

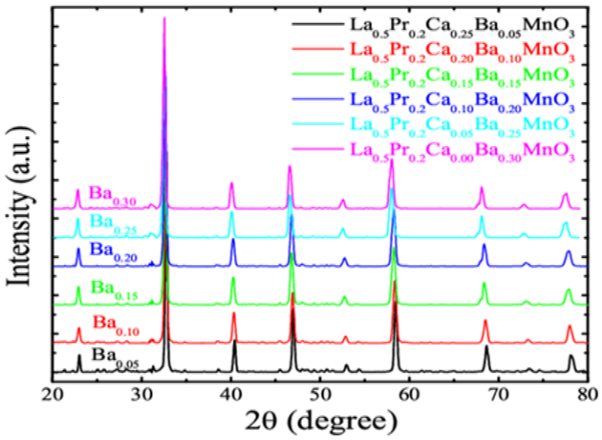

Fig. 1: *XRD Patterns of $La_{0.5}Pr_{0.2}Ca_{0.3-x}Ba_xMnO_3$ (LPCBMO) (x = 0.05, 0.10, 0.15, 0.20, 0.25 and 0.30) Manganites.*

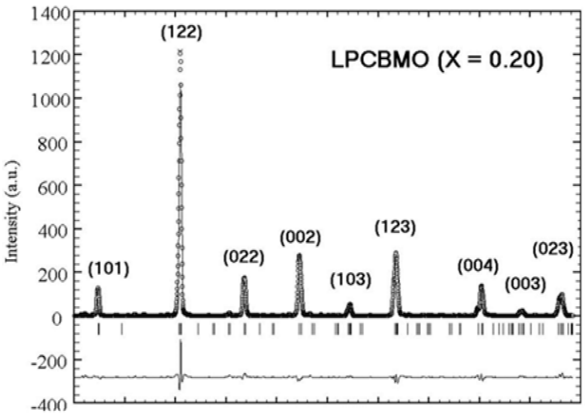

Fig. 2: *Typical Rietveld Refined XRD Pattern of $La_{0.5}Pr_{0.2}Ca_{0.3-x}Ba_xMnO_3$(x = 0.20) Manganite Compound.*

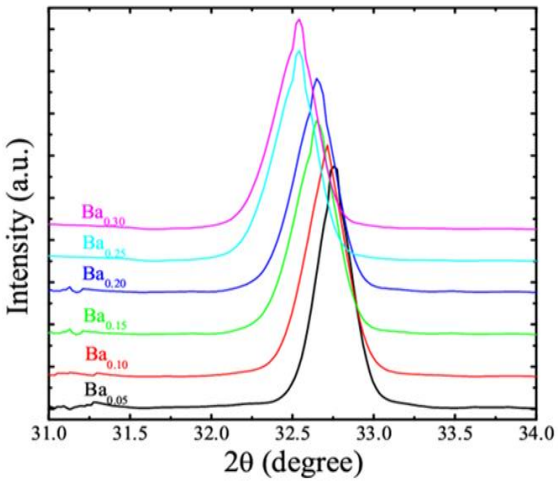

Fig. 3: *Enlarged View of Most Intense 122 Peaks of XRD Patterns of $La_{0.5}Pr_{0.2}Ca_{0.3-x}Ba_xMnO_3$ (LPCBMO) (x = 0.05, 0.10, 0.15, 0.20, 0.25 and 0.30) Manganites.*

The crystallite size (CS) has been calculated using Scherer's formula: $CS = 0.9\lambda/B\cos\theta$; where λ is the wave length of X-ray, B is the FWHM of XRD peak and θ is the Bragg's angle. It is found that with increase in x, CS decreases from 76 nm ($LPCB_{0.05}MO$) to 13 nm ($LPCB_{0.30}MO$). All the samples studied possess nanocrystalline nature having the CS << 100 nm which can be attributed to prolonged grinding of the samples during synthesis process. The variation in CS with x can be understood as – with increase in x, the value of size disorder, one of the effective structural parameters [9, 10], increases from 3.81×10^{-5} ($LPCB_{0.05}MO$) to 14.9×10^{-5} ($LPCB_{0.30}MO$) due to large size mismatch between Ca^{2+} and Ba^{2+}, which controls the crystallinity in the samples substituted with higher concentration of larger Ba^{2+} ion. This in turn results into the large number of crystallite boundaries and smaller CS in higher-doped samples.

In order to understand the interplay between the size disorder, CS and Ba-content (x) and its effect on the transport properties of nanostructured LPCBMO samples, the authors have carried out resistivity measurements in the temperature range of 5–330 K. Figure 5 shows the R–T plots of all the samples under study (except x = 0.20). It is clear that all the samples exhibit metal (at low temperature below peak in resistance) to insulator (at high temperature above peak in resistance) transition at temperature T_P. The resistance decreases from x = 0.10 to x = 0.30. The variation in resistance in not clear for x = 0.05 and 0.10. The decrease in resistance from x = 0.10 to x = 0.30 can be understood as – since the CS decreases from 58 nm (x = 0.10) to 13 nm (x = 0.30) the number of non-crystalline (amorphous type) crystallite boundaries increases which results into the scattering of the charge carriers at the crystallite boundaries and hence increase in resistance, in addition to the structural disorder induced increase in deteriorated transport and conduction process. Unlikely, the picture is different in the present case, i.e., with increase in Ba-content (x), the resistance decreases which is ascribed to the Ba-content (x) induced increase in tolerance factor (t) (Table 2) which enhances the Mn-O-Mn bond angle and supports the transport in the

presently studied manganite system. In the samples having $x \geq 0.10$, the strong competition between disorder and tolerance factor induced modifications in the resistance of the samples results into the effectiveness of the tolerance factor at nanoscale level. In other words, the effect of tolerance factor dominates over the effect of disorder in nanocrystalline LPCBMO samples. In consideration of $x = 0.05$ and $x = 0.10$, the delicate interplay between the effect of structural disorder and tolerance factor indicates that at low and high temperature, the disorder effect is strong enough while around the resistance peak, tolerance effect is found to be prominent.

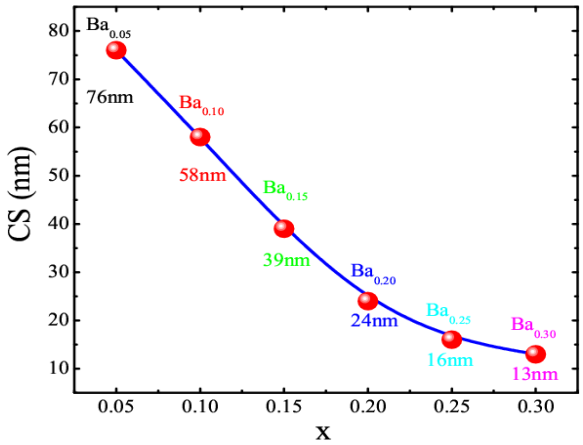

Fig. 4: *Variation in CS with Ba-Content (x) for $La_{0.5}Pr_{0.2}Ca_{0.3-x}Ba_xMnO_3$ (LPCBMO) (x = 0.05, 0.10, 0.15, 0.20, 0.25 and 0.30) Manganites.*

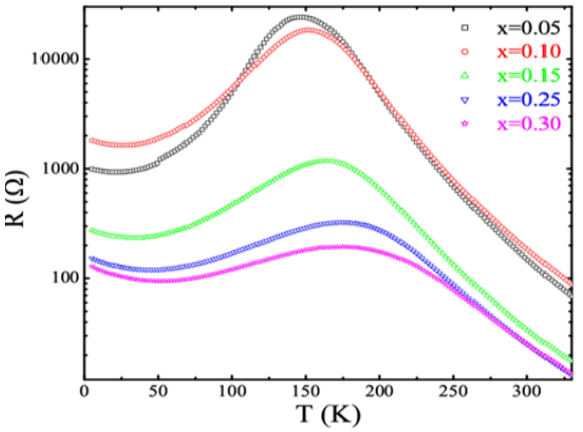

Fig. 5: *Variation in Resistance with Temperature for Nanostructured $La_{0.5}Pr_{0.2}Ca_{0.3-x}Ba_xMnO_3$ (LPCBMO) (x = 0.05, 0.10, 0.15, 0.25 and 0.30) Manganites.*

In addition, to understand the effect of Ba-content (x) on peak resistance (R_P) values and peak resistance temperature (T_{RP}), in Figure 6, the authors have plotted the variation in R_P and T_{RP} with x for all the samples under study except $x = 0.20$. It can be seen that with increase in Ba-content, R_P decreases while T_{RP} increases monotonically which can be attributed to the strong efficiency of tolerance factor effect rather than disorder effect. The increase in T_{RP} with Ba-content (x) is ascribed to the tolerance factor induced improvement in the possibility of Zener double-exchange mechanism in higher doped samples.

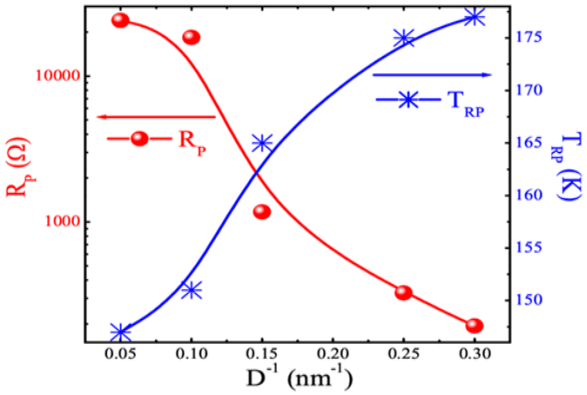

Fig. 6: *Variation in Peak Resistance (R_P) and Peak Resistance Temperature (T_{RP}) for Nanostructured $La_{0.5}Pr_{0.2}Ca_{0.3-x}Ba_xMnO_3$ (LPCBMO) (x = 0.05, 0.10, 0.15, 0.25 and 0.30) Manganites.*

CONCLUSIONS

In summary, the nanocrystalline $La_{0.5}Pr_{0.2}Ca_{0.3-x}Ba_xMnO_3$ (LPCBMO) (x = 0.05, 0.10, 0.15, 0.20, 0.25 and 0.30) manganites using conventional solid state reaction route with prolonged grinding process have been successfully synthesized. This results into the nanocrystalline nature of the samples. With increase in Ba-content (x), CS decreases which is attributed to the size mismatch and hence structural disorder induced structural modifications. The transport studies reveal that with increase in Ba-content (x), the effectiveness of tolerance factor (t) dominates over the structural disorder effect and hence results into the improved transport properties of presently studied nanocrystalline LPCBMO samples. Increase in resistance peak temperature (T_{RP}) is ascribed to the tolerance factor induced improvement in supportive strength of Zener double-exchange mechanism.

Finally, it is seen that at nanoscale level also, the effectiveness of tolerance factor remains existing in the transport mechanism of manganites.

ACKNOWLEDGMENT

The author is thankful to the Government of Gujarat and Saurashtra University, Rajkot, for providing financial assistance from the World Class University Grant for Nanoscience Research.

REFERENCES

1. Baibich MN, Broto JM, Nguyen Van Daw F., et al. *Phys. Rev. Lett.* 1988; 61: 2472p.
2. Ramirez AP. *J. Phys.: Condens. Matter*. 1997; 9: 8171p.
3. Reveau B, Maignan A, Martin C, et al. In: Rao CNR, Raveau B (Eds). *Colossal Magnetoresistance, Charge Ordering and Related Properties of Manganites Oxides*. Singapore: Word Scientific; 1998.
4. Viret M, Ranno L, Coey JMD. *Phys. Rev.* 1997; 55: 8067p.
5. Raychaudhuri P, Nath TK, Nigam AK, et al. *J. Appl. Phys.* 1998; 84; 2048p.
6. Gupta A, Sun JZ. *J. Magn. Magn. Mater.* 1999; 200: 24p.
7. Shah NA. *Appl. Nanosci.* 2013; DOI 10.1007/s13204-013-0272-3.
8. Shah NA. *J. Nanosci. Nanoeng. Applications.* 2013;3:24p.
9. Rathod Jalshikhaba S, Khachar Uma, Doshi RR, et al. *Int. J. Mod. Phys.* 2012; B 26: 1250136.
10. Kansara Sanjay, Pandya DD, Nimavat Bhumika, et al. *Adv. Mater. Res.* 2013; 665: 1p.

Facile Synthesis and Characterization of ZIF-8 Nanocrystals

Girish Mohanta[1,2]*, Sumandeep Kaur[3], Rupesh Kumar[3], A. K. Paul[1,2] and Akash Deep[1,2]
[1]Academy of Scientific and Innovative Research, CSIR-CSIO, Sector 30 C, Chandigarh, 160030, India
[2]Central Scientific Instruments Organisation (CSIR-CSIO), Sector 30 C, Chandigarh, 160030, India
[3]DAV Institute of Engineering & Technology, Jalandhar, Punjab, India

Abstract

Zeolitic imidazolate frameworks (ZIFs) are important subclass of porous metal-organic frameworks (MOFs). The ZIFs structure has zeolitic framework topologies wherein all tetrahedral atoms are transition metal ions and are bridged by imidazolate (IM) units. Zeolitic imidazolate framework-8 (ZIF-8) is a prototypical member of ZIF family, constituted from zinc metal ions and 2-methylimidazole as bridging linkers. ZIF-8 nanocrystals have gained significant research interest in recent past due to its applications in various fields such as gas sensing, gas separation, catalysis and moreover it allows easy fabrication of advanced sensors. Traditionally, syntheses of ZIF-8 nanocrystals have been a challenge and were mostly done in organic solvents which are undesirable due to their environmental and health-associated risks. The authors report here synthesis of (ZIF-8) nanocrystals through simple aqueous route method at room temperature. The synthesis method utilized simple inorganic precursors as starting material and completed within few minutes as against several hours reported in organic solvents. The obtained ZIF-8 nanocrystals were characterized by different characterization techniques like X-ray diffraction, Fourier transformed infrared spectroscopy, dynamic light scattering, energy dispersive X-ray spectroscopy, differential scanning calorimetry and thermo-gravimetric analysis. The synthesis method yielded a homogeneous population of pure phase ZIF-8 nanocrystals with high thermal stability with an average size of around 100 nm.

Keywords: *Metal organic framework, zeolitic imidazolate framework, nanocrystals, aqueous synthesis*

****Author for Correspondence*** E-mail: gmohanta@csio.res.in

INTRODUCTION

Metal-organic frameworks (MOFs), also known as porous coordination networks (PCNs), are crystalline, porous materials constructed from metal ions and organic molecules known as linkers/ligands coordinated in a framework structure. In the 3D framework structure, metal ions act as nodes whereas organic linkers act as spacers and are linked through coordinate bonds [1, 2]. Interestingly, porosity and even the sizes and shapes of the nanosize pores (network topology) can be rationally designed by simple replacements in the framework with appropriate organic linkers and metal ions; a designed synthesis process known as "Reticular Synthesis" [1, 3, 4]. These porous, crystalline MOFs show remarkable properties such has high porosity [5], selective gas adsorption, high thermal and chemical stability, luminescence, and catalytic activity [6, 7]. These remarkable properties have allowed use of MOFs in various applications like gas storage, gas separation, biological and chemical sensing, and as chemical catalysts [8, 9].

Zeolitic imidazole frameworks (ZIFs) are an important class of MOFs which derive their name from inorganic zeolites due to their structural resemblance. ZIF structure primarily consists of Zn ion, or in some cases Co or Cu ions, as metal centers and imidazole organic linker (or its derivative), coordinated together

in a stable 3D framework. Inorganic zeolites on the other hand consist of tetrahedral $Si(Al)O_4$ units covalently linked through oxygen atoms. Interestingly, the bond angle of 145° made by imidazole and zinc metal ions (M-Im-M; Im = imidazole, M = metal ions) in ZIF structure resembles the Si-O-Si bond angles present in zeolite structure, suggesting that ZIFs acquire the zeolite-type structure [10–12]. Inorganic zeolites offer excellent properties such as high porosity, high chemical and thermal stability, structural diversity and catalytic activity, due to which zeolites have been employed in different industrial applications such as petroleum cracking, ion exchange for water softening and purification, separation of gases and heterogeneous catalysis [12–15].

Due to their designable pore size, shape and structural diversity, the zeolitic porous materials are emerging as a new class of functional materials that find numerous applications. Choice of metal ion and organic linker gives almost limitless possibilities of various network topologies and thereby associated properties. The ZIFs combine properties of both zeolites and MOFs such as structural tunability, monodispersed microporosity, ultrahigh surface areas, structural flexibility and chemical, thermal and hydrothermal stability, which are highly desirable for industrial applications [12,16–18]. Various types of ZIFs and their structural resemblance with zeolite-type structures have been widely covered in the literature [19, 20].

ZIF-8 is a protypical member of ZIF family, consisting of zinc metal ions and 2-methyl imidazole as organic linkers, coordinated in a sodalite-type of zeolitic network topology. Among various types of ZIFs, ZIF-8 has particularly gained increased research interest due to its high porosity, high surface area (~ 2000 m^2/g), large pore size (diameter 11.6 nm) and higher chemical and thermal stability as compared with other MOFs [12, 16, 21]. The pores of ZIF-8 are of particular interest due to their large size and narrow window (~ 3.4 nm), which is desirable in gas storage, separation and catalysis applications [22]. Recently, nanocrystallite ZIF-8 has gained research interest due to its easy fabrication into sensor platform and enhanced surface properties [23]. However, early synthesis of ZIF-8 nanocrystals is reported in organic solvents such as dimethylformamide (DMF), diethylformamide (DEF), and methanol which causes environmental pollution, which are costly and may not be feasible for industrial scale synthesis [24].

In this paper has been reported a facile aqueous route synthesis of ZIF-8 nanocrystals using inexpensive inorganic salts as starting precursors. These synthesized ZIF-8 nanocrystals were characterized using X-ray diffraction (XRD), field emission scanning electron microscopy (FE-SEM), energy dispersive X-ray spectroscopy (EDX), Fourier transformed infrared spectroscopy (FTIR), dynamic light scattering (DLS) and differential scanning calorimetry (DSC) and thermo-gravimetric analysis (TGA).

EXPERIMENTAL

Materials and Methods

All the reagents used were of analytical grade or of the highest purity available and were used as obtained without further purification. The ZIF-8 nanocrystals were synthesized from zinc chloride dry ($ZnCl_2$, MW 136.29) and 2-methylimidazole precursors as follows. Firstly, 0.248 g $ZnCl_2$ (~ 40 mM) was dissolved in 4 mL of deionized (DI) water. Separately, 11.35 g 2-methylimidazole (~ 3 M) was dissolved in another 40 mL DI water by stirring. The above two solutions were slowly mixed with continuous stirring. The reaction mixture turned milky instantly, and it was then left for 10 min for the reaction to complete. All steps were performed at room temperature (25 ± 2 °C). Finally, the white precipitate was collected by centrifugation at 15000 rpm for 15 min, followed by repeated washing with DI water. Washing was done to remove any unreacted organic part or any other impurities. The precipitate was dried overnight in a hot air oven at 65 °C and then grounded to obtain fine powder and stored for further characterizations.

Characterization Techniques

X-Ray diffraction (XRD) pattern of the powder sample was recorded using X'Pert3 X-Ray diffractometer (PANalytical) with Cu Kα emission (λ = 1.5406 Å) and 2θ range of 5 to 35°. Functional group analysis of the powder

sample was done using FTIR spectrophotometer from Thermo Fisher Scientific (model Nicolet iS10) using potassium bromide pallet. FE-SEM/EDX analysis of the powder sample was done on Hitachi S4300 system at 18 kV accelerating voltage keeping 7.7 mm of working distance. Particle size distribution of the sample was recorded on Malvern DLS system after its dispersion in methanol. TGA and DSC investigations were performed on Thermal Analysis SDT Q600 instrument.

RESULTS AND DISCUSSIONS

Previous works reported on ZIF-8 nanocrystal synthesis primarily used organic solvents, which are undesirable for bulk-scale synthesis due to their environmental- and health-associated factors [10]. Some recent reports on the aqueous route synthesis emphasized the requirement of a high metal to organic linker ratio to obtain ZIF-8 particles in nanosize regime [16, 25]. Keeping this in view, the authors have synthesized ZIF-8 nanocrystals using zinc chloride ($ZnCl_2$) and 2-methylimidazole in a molar ratio of 1:75 in DI water at room temperature. The ZIF-8 nanocrystal formation took place rapidly and pure phase product was precipitated out of the solution, which required no further purification in contrast to organic solvent-based method [25, 26]. The ZIF-8 nanocrystals were obtained as white precipitates, which were dried in the oven and grounded to powder before further characterization.

The ZIF-8 nanocrystals were characterized by variety of techniques. Figure 1 shows X-ray diffraction patterns of the as-synthesized ZIF-8 nanocrystals. The prominent peak-broadening effect and sharp diffraction peaks indicated crystalline nature and nanoscale regime of synthesized ZIF-8. The overall XRD pattern obtained for ZIF-8 nanocrystals is in good agreement with previously reported literature [26, 27]. The XRD planes observed (indexed) belong to sodalite type (SOD) topology of zeolites [10].

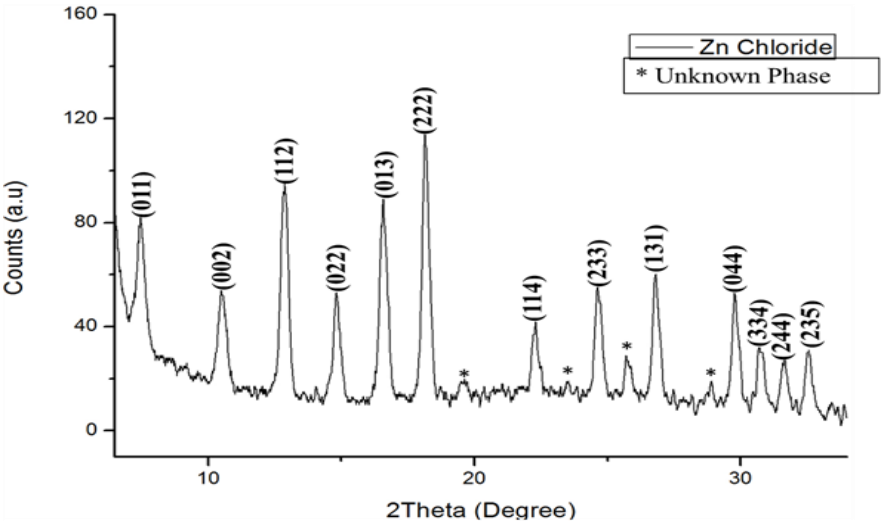

Fig. 1: *XRD Pattern of as-Synthesized ZIF-8 Nanocrystals.*

Figure 2 shows FTIR spectra of ZIF-8 nanocrystals to reveal the functional groups present on the surface of the nanocrystals. The absorption band at 2926 cm^{-1} is associated with the aliphatic C-H stretch of the imidazole. The peak at 1567 cm^{-1} can be assigned as the C = N stretch mode, whereas the intense and convoluted bands at 1300–1500 cm^{-1} are associated with the entire imidazole ring stretching. The bands in the spectral region of 900–1350 cm^{-1} are attributed to *in-plane* bending of the ring while those below 800 cm^{-1} are assigned as *out of plane*. The peak obtained at 424 cm^{-1} can be assigned to Zn-N stretching mode indicating coordinated zinc metal ions and 2-methylimidazole linkers in the framework [28, 29].

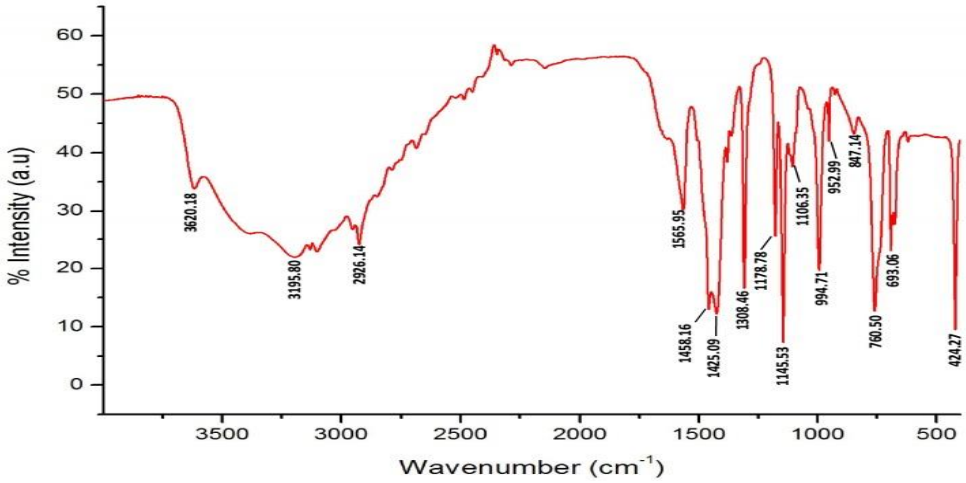

Fig. 2: *FTIR Spectra of ZIF-8 Nanocrystals.*

The particle size and particle size distribution is measured through DLS technique as shown in Figure 3. The DLS measurement was carried out on methanol dispersed sample and shows an average size of 122 nm for synthesized ZIF-8 nanocrystals with polydispersity index (PDI) of 0.077, indicating uniform size distribution of the particles. The Gaussian nature of the DLS curve also suggests that no other secondary population (bulk sized) of ZIF-8 was co-synthesized and the reaction condition completely favors the formation of nanosized ZIF-8 nanocrystals.

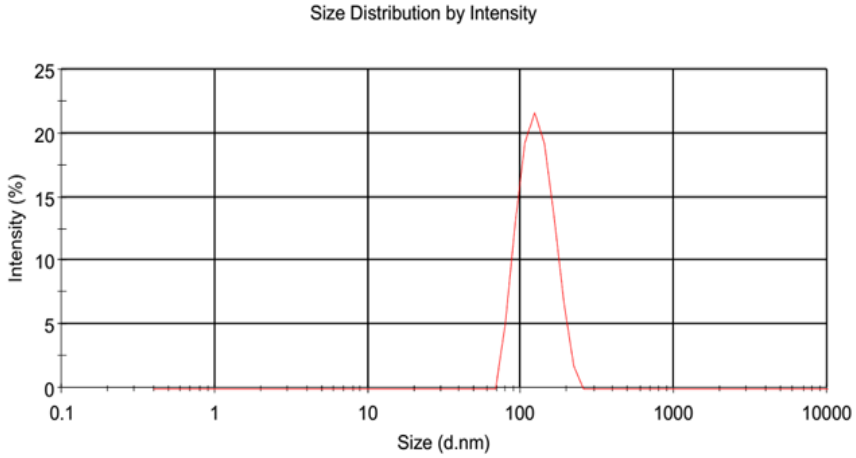

Fig. 3: *DLS Measurement of ZIF-8 Nanocrystals.*

The observation from the DLS was further validated through FESEM micrograph shown in Figure 4 indicating size of ZIF-8 nanocrystals to be around 100 nm. The size observed in FESEM micrograph varies from that reported in the DLS measurement possibly because DLS measurement reports the complete hydrodynamic size (solvent layer) of the nanocrystals whereas in FESEM micrograph, actual size of the nanocrystals is visualized. Compositional analysis of the synthesized ZIF-8 nanocrystals was done through EDX and the representative spectrum is shown in Figure 5. The EDX spectra shows presence of peaks for C, N, O and Zn as expected which indicates that the product obtained was indeed having pure phase and was not altered with any impurity. The peak for Si arises due to Si-wafer used for deposition of the ZIF-8 nanocrystal for FESEM and EDX. Presence of oxygen could be due to bound solvent molecules (H_2O).

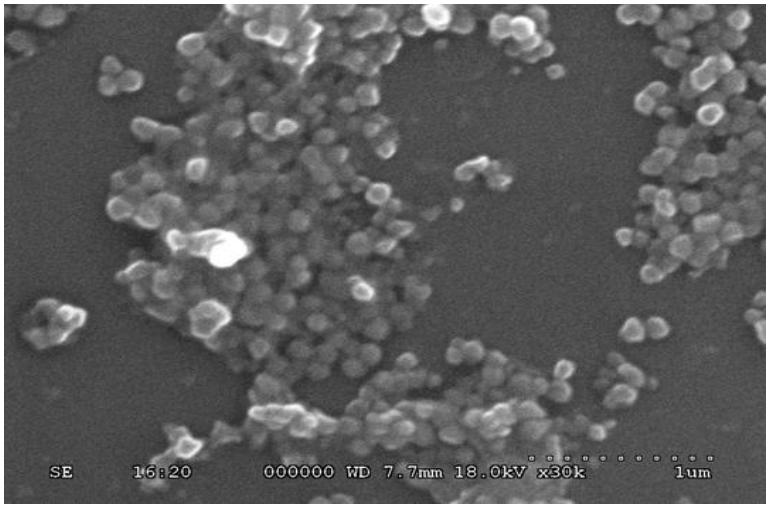

Fig. 4: *SEM Micrograph of Synthesized ZIF-8 Nanocrystals.*

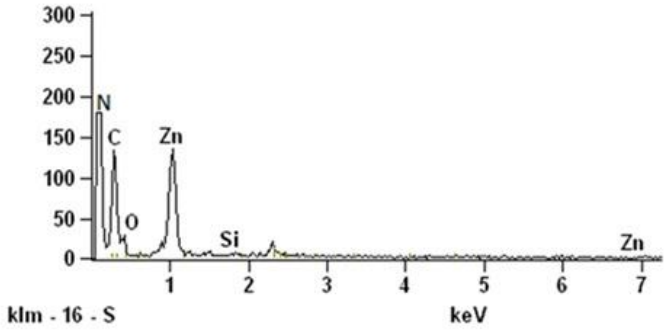

Fig. 5: *EDS Spectra of ZIF-8 Nanocrystals.*

Finally, thermal stability of the synthesized ZIF-8 nanocrystals was characterized through TGA-DSC measurement. Figure 6 shows the TGA (green) and DSC (blue) curve of the as-synthesized ZIF-8 nanocystals. The TGA curve of the synthesized ZIF-8 nanocrystals shows three major gradual transitions (phases) with respect to percent weight loss as a function against temperature increase. The first transition of gradual weight loss step of around 6.2% takes place from ambient temperature to 80 ºC, which could be attributed to removal of surface bound water molecules (moisture) and loosely held guest molecules (water). Second transition occurs from 80 to 222 ºC during which around 23% weight loss is observed. This could be due to the removal of tightly bound water molecules, unreacted organic linkers and/or adsorbed gases from the framework structure. In the third transition at temperature above 222 ºC, the curve shows a nearly plateau region up to around 450 ºC, beyond which it abruptly falls to a total weight loss of ~ 53% indicating collapse of the framework structure. In all, a total weight loss of around 62.5% has been observed between the ambient and 500 ºC temperature suggesting that ZIF-8 framework collapses and yields zinc oxide (ZnO) as a possible byproduct [21].

DSC curve (Figure 6) shows an exothermic peak around 450 ºC which coincides with the TGA dissociation curve for the ZIF-8 framework, thus supporting the abrupt framework collapse as indicated by the TGA curve. It is interesting to note that DSC curve did not show any significant change during the first (at 80 ºC) and second transition (at 222 ºC) temperature which indicates that these transitions were indeed because of removal of unbound organic linkers and tightly held guest molecules and the framework remained thermally stable at these temperatures.

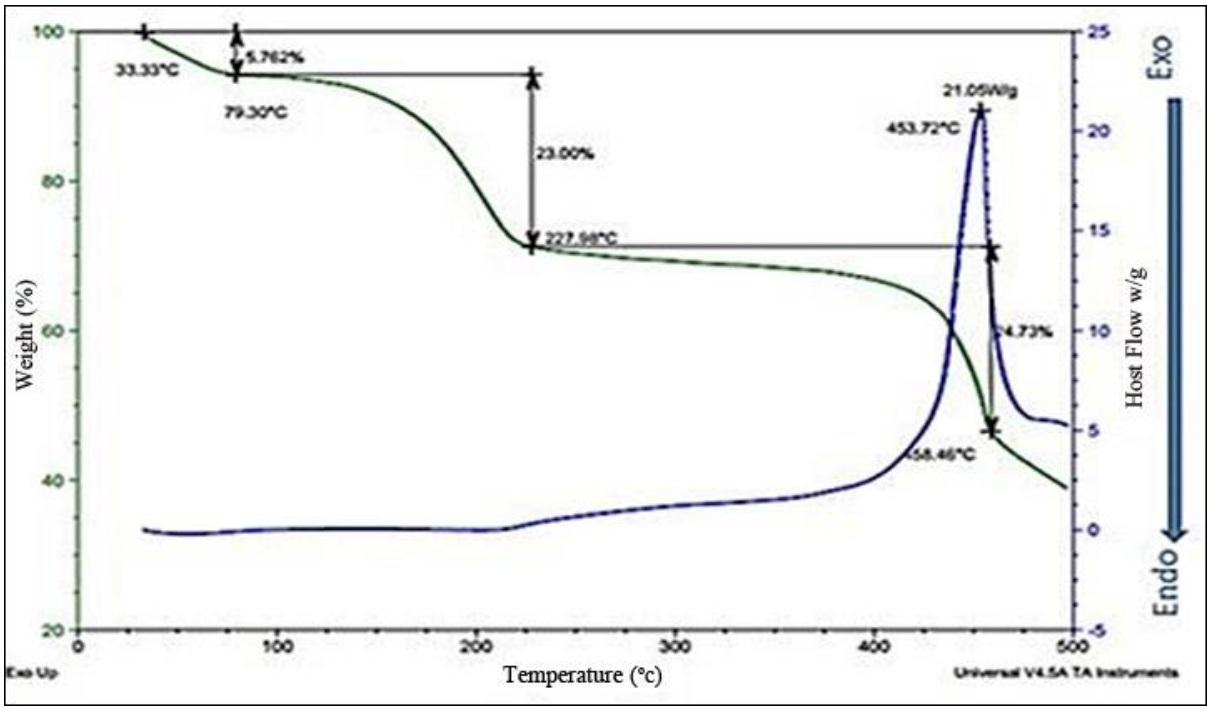

Fig 6: *DSC-TGA Curve for ZIF-8 Nanocrystals*

CONCLUSIONS

The authors have synthesized ZIF-8 nanocrystals through simple aqueous route, room temperature method within a few minutes. The obtained ZIF-8 nanocrystals were in pure phase and did not require any further purification. Structural and functional characterization confirmed synthesis of crystalline ZIF-8 nanocrystals with average crystallite size of around 120 nm. Thermal properties of the synthesized ZIF-8 nanocrystals showed framework stability up to 450 °C, beyond which it breaks down exothermically. The proposed synthesis route could be scaled up to industrial level as it utilizes inexpensive inorganic precursor, time saving and results in homogeneous population of ZIF-8 nanocrystals.

ACKNOWLEDGMENTS

Reported work has been funded through CSIR, India grant (OMEGA/PSC0202/2.2.5) from CSIR, India. The authors are also grateful to the Director, CSIR-CSIO, Chandigarh, for providing research facilities.

REFERENCES

1. Cook TR, Zheng Y-R, Stang PJ. Metal–organic frameworks and self-assembled supramolecular coordination complexes: Comparing and contrasting the design, synthesis, and functionality of metal–organic materials. *Chem Rev*. 2012; 113(1): 734–77p.
2. Li J-R, Sculley J, Zhou H-C. Metal-organic frameworks for separations. *Chem Rev*. 2011. 112(2): 869–932p.
3. Goto Y, et al. Clickable metal−Organic framework. *J Am Chem Soc.* 2008; 130(44): 14354–5p.
4. Yaghi OM, et al. Reticular synthesis and the design of new materials. *Nature*. 2003; 423(6941): 705–14p.
5. Furukawa H, et al. Ultrahigh porosity in metal–organic frameworks. *Science*. 2010; 329(5990): 424–8p.
6. NW Ockwig, et al. Reticular chemistry: Occurrence and taxonomy of nets and grammar for the design of frameworks. *Accounts Chem Res*. 2005; 38(3): 176–82p.
7. Meek ST, Greathouse JA, Allendorf MD. Metal–organic frameworks: A rapidly growing class of versatile nanoporous materials. *Adv Mater*. 2011. 23(2): 249–67p.
8. Kuppler RJ, et al. Potential applications of metal–organic frameworks. *Coordin Chem Rev*. 2009; 253(23–24): 3042–66p.
9. Keskin S, Kızılel S. Biomedical applications of metal organic frameworks. *Ind Eng Chem*. 2011; 50(4): 1799–1812p.

10. Venna SR, Jasinski JB, Carreon MA. Structural evolution of zeolitic imidazolate framework–8. *J Am Chem Soc*. 2010; 132(51): 18030–3p.
11. Phan A, et al. Synthesis, structure, and carbon dioxide capture properties of zeolitic imidazolate frameworks. *Accounts Chem Res*. 2009; 43(1): 58–67p.
12. Park KS, et al. Exceptional chemical and thermal stability of zeolitic imidazolate frameworks. *Proceedings of the National Academy of Sciences*. 2006; 103(27): 10186–91p.
13. Bellussi G, Carati A, Millini R. Industrial potential of zeolites, in zeolites and catalysis. Wiley–VCH Verlag GmbH & Co. KGaA; 2010; 449–91p.
14. Centi G, Perathoner S. Environmental catalysis over zeolites, in zeolites and catalysis. Wiley–VCH Verlag GmbH & Co. KGaA; 2010; 745–74p.
15. Rigutto M. Cracking and hydrocracking. In: *Zeolites and Catalysis*. Wiley–VCH Verlag GmbH & Co. KGaA; 2010; 547–84p.
16. Tanaka S, et al. Size–controlled synthesis of zeolitic imidazolate framework–8 (zif–8) crystals in an aqueous system at room temperature. *Chemistry Letters*. 2012. 41(10): 1337–9p.
17. Kitagawa S, Kitaura R, Noro S–i. Functional porous coordination polymers. *Angewandte Chemie*, International Edn. 2004; 43(18): 2334–75p.
18. Huang X–C, et al. Ligand–directed strategy for zeolite–type metal–organic frameworks: zinc (II) imidazolates with unusual zeolitic topologies. *Angewandte Chemie*, International Edn. 2006; 45(10): 1557–9p.
19. Thompson JA, et al. Sonication–induced ostwald ripening of zif–8 nanoparticles and formation of zif–8/polymer composite membranes. *Microporous and Mesoporous Materials*. 2012; 158(0): 292–9p.
20. Lewis DW, et al. Zeolitic imidazole frameworks: structural and energetics trends compared with their zeolite analogues. *Cryst Eng Comm*. 2009; 11(11): 2272–6p.
21. Kida K, et al. Formation of high crystalline ZIF–8 in an aqueous solution. *Cryst Eng Comm*. 2013; 15(9): 1794–1801p.
22. Hideki H, et al. Zeolite A imidazolate frameworks. *Nature Materials*. 2007; 6(7): 501–6p.
23. Nune SK, et al. Synthesis and properties of nano zeolitic imidazolate frameworks. *Chemical Communications*. 2010; 46(27): 4878–80p.
24. Cravillon J, et al. Rapid room–temperature synthesis and characterization of nanocrystals of a prototypical zeolitic imidazolate framework. *Chem Mater*. 2009; 21(8): 1410–2p.
25. Pan Y, et al. *Rapid synthesis of zeolitic imidazolate framework–8 (ZIF–8) nanocrystals in an aqueous system. Chemical Communications*. 2011; 47(7): 2071–3p.
26. Nguyen LTL, Le KKA, Phan NTS. A zeolite imidazolate framework ZIF–8 catalyst for Friedel–Crafts acylation. *Chinese Journal of Catalysis*. 2012; 33 (4–6): 688–96p.
27. Gross AF, Sherman E, Vajo JJ. Aqueous room temperature synthesis of cobalt and zinc sodalite zeolitic imidizolate frameworks. *Dalton Transactions*. 2012; 41(18): 5458–60p.
28. Hu Y, et al. In situ high pressure study of ZIF–8 by FTIR spectroscopy. *Chemical Communications*. 2011; 47(47): 12694–6p.
29. Song Q, et al. Zeolitic imidazolate framework (ZIF–8) based polymer nanocomposite membranes for gas separation. *Energy & Environmental Science*. 2012; 5(8): 8359–69p.

Silver Nanoparticles Incorporated Soy Protein and Chitosan based Biomaterials

Rakesh Kumar*
Department of Applied Chemistry, Birla Institute of Technology, Mesra, Patna Campus, Patna, India

Abstract

Chitosan and soy protein are abundantly available renewable biopolymers. The combination of the nano-sized powders and the biopolymer matrix will result in the formation of bio-nanocomposites. Due to bactericidal properties, silver nanoparticles are widely used in the medical applications. Chitosan and soy protein based bio-nanocomposites can be fabricated by incorporating silver nanoparticles in the biopolymer matrix. The bio-nanocomposites fabricated can be used as antimicrobial packaging which can be considered as an emerging technology that could have a significant impact on life and food safety. Antimicrobial agents in food packaging can control the microbial population and target specific microorganisms to provide greater safety and higher quality products. This newly developed material, discussed in this review paper, thus has potential for use in food and medical industries as well as in biomedical fields. The bio-nanocomposites can also find economically viable applications in water purification technology and in biotechnology.

Keywords: *Chitosan, soy protein, silver nanoparticles, wound dressing*

****Author for Correspondence*** E-mail: krrakesh72@gmail.com

INTRODUCTION

Silver (Ag) has been known to have bactericidal properties and silver compounds have been exploited for their medicinal properties for centuries as well [1]. Before the advent of antibiotics in the early part of the 20th century, silver were popular remedies for tetanus and rheumatism as well as for colds and gonorrhea [2]. At present, silver has re-emerged as a viable treatment option for infections encountered in burns, open wounds, and chronic ulcers.

Several products have incorporated silver for use as a topical antibacterial agent, such as silver nitrate, silver sulphadiazine (SSD) [3] and silver sulphadiazine/chlorhexidine [4]. About 0.5% concentration of silver nitrate is the standard and most popular silver salt solution used for topical burn wound therapy. Concentrations exceeding 1% silver nitrate are toxic to the tissues. Silver sulfadiazine was introduced long back in 1970s. Silver is complexed to propylene glycol, stearyl alcohol, and isopropyl myrislate and mixed with the antibiotic sulfadiazine producing a combined formulation made from silver nitrate and sodium sulphadiazine [5, 6]. Then these compositions are used as an antibacterial agent for topical treatment of burns and wounds.

The uses of Ag-based antiseptics are being preferred to antibiotics so as to induce microbial resistance that may be linked to broad-spectrum activity and far lower propensity [7]. Silver is currently used to control bacterial growth in a variety of applications, including dental work, catheters, and burn wounds [8, 9]. Reducing the particle size of silver materials is an efficient and reliable tool for improving their biocompatibility. The antimicrobial effects of Ag nanoparticles against representative microorganisms have been investigated in detail by several researchers. Several mechanisms have been postulated for the antimicrobial property of silver nanoparticles and they are listed below:

a. Adhesion of nanoparticles to the surface altering the membrane properties. Silver nanoparticles have been reported to degrade lipopolysaccharide molecules that

accumulate inside the membrane by forming ''pits'', and cause large increases in membrane permeability [10].

b. Silver nanoparticles penetrating inside bacterial cell, resulting in DNA damage.
c. Dissolution of silver nanoparticles releases antimicrobial Ag^+ ions [11].

Physicochemical properties play an important role in the antimicrobial activity of silver nanoparticles. In general, particles of less than 10 nm are more toxic to bacteria such as *Escherichia coli* and *Pseudomonas aeruginosa* [12, 13]. Silver nanoparticles ranging from 1 to 10 nm inhibit certain viruses from binding to host cells [14].

There are several reports of silver nanoparticles incorporated cellulose and polylactide based biopolymers [15, 16]. Cellulose is able to bind electropositive transition metal atoms such as silver by electrostatic interactions. Consequently, Ag^+ ions are adsorbed by cellulose during immersion in silver nitrate [17].

But little is published to show the incorporation of silver nanoparticles in soy protein as well as chitosan based biopolymers. Though chitosan has strong affinity toward silver ions, due to the presence of amine and hydroxyl groups [18], and is able to reduce Ag^+ ions to silver nanoparticles under alkaline conditions [19]. Considering the affinity of silver to sulphur compounds such as the amino acid cysteine, Zhang et al., prepared silver-protein nanocomposites by dispersing solutions of α-lactalbumin (ALA), a high cysteine protein, in $AgNO_3$ solutions [20]. The nanocomposites were formed by Ag-S or Ag-N electrostatic attraction and coordination bonds. Ag affinity to sulfur depends strongly on the redox state of cysteine. In view of above concept, we are reporting here the review related to the incorporation of silver nanoparticles in chitosan and soy protein.

PREPARATION/SYNTHESIS OF SILVER NANOPARTICLES

There are several methods to prepare/synthesize silver nanoparticles [21, 22]. They are chemical reduction, thermal decomposition, laser ablation, and sonochemical method. Chemical reduction methods are the most commonly employed method. In this section, we give the details of one of the method. In this method, aqueous solution of 1.0×10^{-3} M silver nitrate was mixed with an aqueous solution of 2.0×10^{-3} M sodium borohydride. By mixing both solutions at low temperature, Ag ions were reduced and clustered together to form monodispersed nanoparticles as a transparent sol in aqueous medium. The solution was stirred repeatedly for approximately an hour until it became stabilized and thus stable Ag nanoparticles were formed. Figure 1 shows the UV-Vis and TEM (Transmission Electron Microscopy) characterization of the synthesized Ag nanoparticles. The prepared aqueous solution of Ag nanoparticles showed an absorption band at 391 nm, which is a typical absorption band of spherical Ag nanoparticles [23] as shown in Figure 1a. The TEM image of silver nanoparticles is shown in Figure 1b.

Silver nanoparticles were also synthesized with the aid of a novel, non-toxic, eco-friendly biological material, namely aloe leaf extract (ALE) [24]. In this research paper crushed, ultrasound treated, decolorized aqueous aloe leaf extract was used for capping silver nitrate. Silver nanoparticles were formed when the reaction conditions were altered with respect to concentration of silver nitrate, consumption of hydrazine hydrate, ALE content and incubation temperature. The colorless reaction mixtures turned brown and displayed UV–visible spectra characteristic of silver nanoparticles as shown in Figure 1a. Calvo et al., [25] demonstrated that nanoparticles can elicit a negative tactic response in bacteria at low but environmentally relevant, sublethal concentrations. They suggested that there are likely to be different mechanisms by which nano-scale silver and macro-forms of silver induce a repellent response.

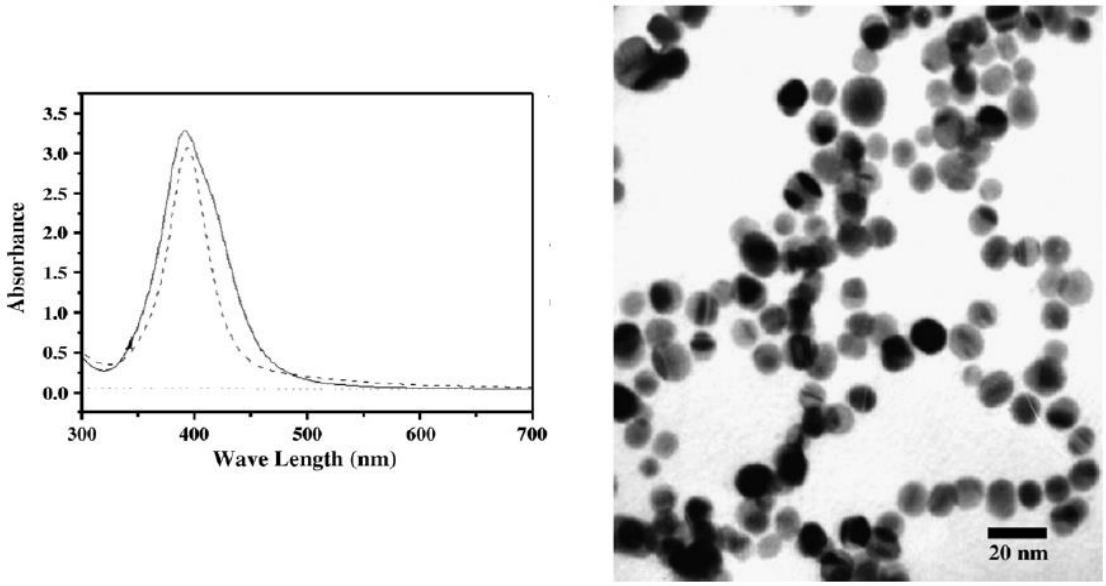

(a) *(b)*

Fig. 1: *Absorption Spectra (a) and TEM Image of Ag Nanoparticles. (Reprinted from Ref. [23] Kim J. S. et al. Nanomedicine: Nanotechnology, Biology, and Medicine 2007; 3: 95p).*

SILVER NANOPARTICLES INCORPORATED CHITOSAN MATERIALS

A green approach based on electrochemical oxidation/complexation process followed by UV irradiation reduction has been reported for the development of stabilized and densely dispersed chitosan-silver nanoparticles [26]. In this case also, the formation of the nanoparticles was confirmed by appearance of surface plasmon absorption around 420 nm. However, the value was slightly higher than that reported in Reference 23. This may be attributed to difference in the synthesis methods. It has been reported that increasing the Ag content in the chitosan-Ag based films tends to decrease their equilibrium swelling values. The silver nanoparticles demonstrated a relatively high antibacterial activity against *Bacillus thuringiensis* and *Pseudomon as aeruginosa* bacteria as compared to that of chitosan and the antibacterial activity increased with increasing the nanoparticle concentration. A novel wound dressing composed of nano-silver and chitosan was reported by Lu et al., [27]. Silver sulfadiazine and chitosan film dressings were used as controls. Compared with the controls, the silver nanocrystalline chitosan dressing significantly increased the rate of wound healing and was associated with silver levels in blood and tissues lower than levels associated with the silver sulfadiazine dressing (Figure 2).

There are several reports where in addition to chitosan some other polymers have also been included. One of the studies investigates the feasibility of a novel nanocomposite (GC/Ag) of a genipin-crosslinked chitosan (GC) film in which various amounts of Ag nanoparticles was embedded. The application intended was wound-dressing [28]. In another work, a lactic acid grafted chitosan film was synthesized. Silver nanoparticles were loaded into the chitosan lactate (CL) film by equilibration in a silver nitrate solution, which was followed by citrate reduction. The silver-nanoparticle-loaded CL film was investigated for its antimicrobial properties against *Escherichia coli* [29]. A thermosensitive poly(*N*-isop-ropyl acrylamide-*co*-vinyl pyrrolidone)/ chitosan [P(NIPAM-*co*-NVP)/CS] semi-interpenetrating (semi-IPN) hydrogels were prepared by redox-polymerization using *N*,*N*-methylenebisacrylamide as crosslinker and ammonium persulfate/*N*,*N*,*N*′,*N*′-tetramethylethylenediamine as initiator [30]. Highly stable and uniformly distributed Ag nanoparticles were prepared by using the

semihydrogel networks as templates via *in situ* reduction of silver nitrate in the presence of sodium borohydride as a reducing agent. Introduction of chitosan improves the hydrogels swelling ratio (SR) and stabilizes the formed Ag nanoparticles in networks.

A bio-composite scaffold containing chitosan/nano-hydroxyapatite/nano-silver particles (CS/nHAp/nAg) was developed by freeze drying technique, followed by introduction of silver ions in controlled amount through reduction phenomenon by functional groups of chitosan [31]. CS/nHAp/nAg bio-composite scaffolds have the potential in controlling implant associated bacterial infection during reconstructive surgery of bone. Its effect on preservation quality of longan fruits (*Dimocarpus longan*) was investigated under ambient temperature. Chitosan/nano-silica coating might provide an attractive alternative to improve preservation quality of fresh longan fruits during extended storage.

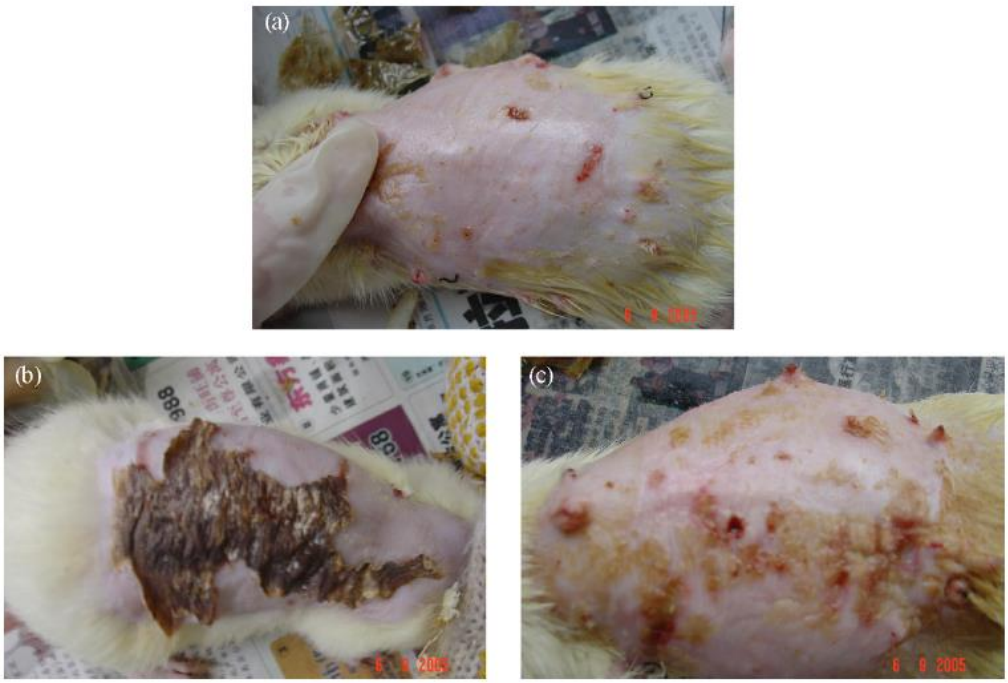

Fig. 2: *Wound Healing Conditions of Rabbit after 10 days: Silver Nanocrystalline Chitosan Dressing (a) Silver Sulfadiazine Dressing (b) and Chitosan Dressing (c). (Reprinted from Ref. [27] Lu. S. et al. Burns 2008; 34: 623p).*

SILVER NANOPARTICLES INCORPORATED SOY PROTEIN MATERIALS

Sun et. al., prepared bactericidal films developed from soy protein isolate (SPI) based film-forming dispersions (FFDs) for use in the food and medical fields [32]. The FFD and films were prepared after the incorporation of different concentrations of $AgNO_3$ as a bactericidal agent. The transparency, tensile strength, and antimicrobial features were evaluated. The opacity of these FFD was greatly decreased after the incorporation of $AgNO_3$. The minimum inhibitory concentration of $AgNO_3$ was 336 μg/mL FFD for both *Escherichia coli* ATCC 25923 and *Staphylococcus aureus* ATCC 25922. An antimicrobial silver nanoparticles (AgNPs) embedded soy protein isolation (SPI) film was prepared by Zhao et al., [33] (Figure 3). AgNPs were *in situ* synthesized from SPI/$AgNO_3$ solution, taking the advantage of the reducibility of tyrosine residue in SPI. The whole reaction process was highly energy-efficient and eco-friendly. The SPI/AgNPs films were prepared by blending *in situ* synthesized AgNPs in SPI solution and additional pristine SPI solution, which showed an effective antimicrobial activity against both Gram-positive and Gram-negative bacteria.

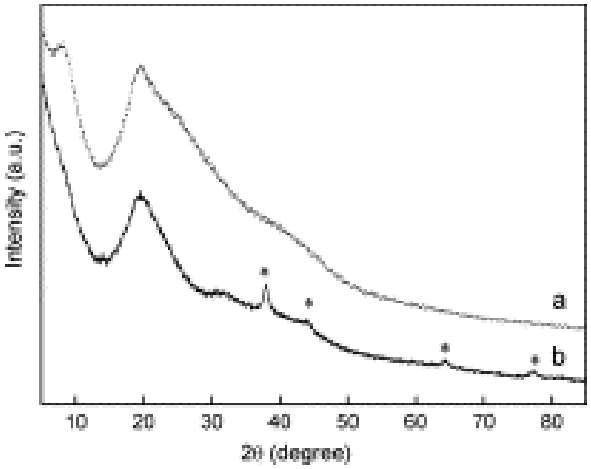

Fig. 3: *XRD Spectra of Ag Nanoparticles and SPI Embedded in Ag Nanoparticles. (Reprinted from Ref. [33] Zhao S. et al. Materials Letters 2013; 95: 142p).*

Zhang et al., used solution blowing to form soy protein-containing nanofibers which were decorated with silver nanoparticles [34]. These nanofibers demonstrated significant antibacterial activity against *E. coli* colonies without exposure to UV light (Figure 4).

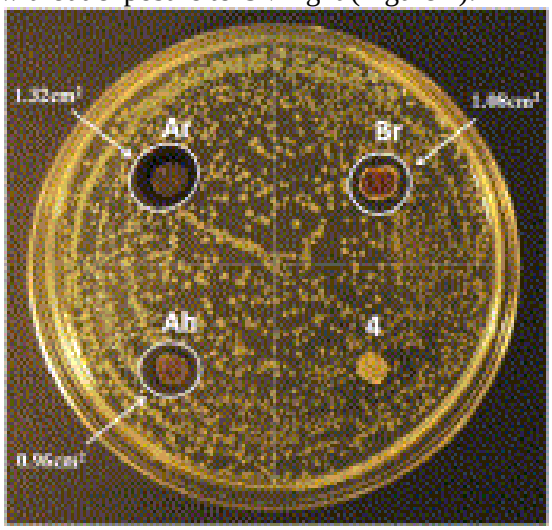

Fig. 4: *Inhibition of E. coli by Silver-Decorated Soy Protein Nanofiber Mats. (Reprinted from Ref. [34] Zhang Y. et al. Catalysis Communications 2013; 34: 35p).*

APPLICATIONS

Food quality and safety are major concerns in the food industry. Antimicrobial packaging can be considered an emerging technology that could have a significant impact on life and food safety. Antimicrobial agents in food packaging can control the microbial population and target specific microorganisms to provide greater safety and higher quality products. Silver nanoparticles incorporated chitosan nanocomposites showed strong antibacterial properties and thus has potential for use as an antibacterial food-packaging material. Silver nanoparticles incorporated chitosan can also be used in burn management and wound healing as well as epithelization as soon as possible in order to prevent infection and to reduce functional and aesthetic after effects. The soy protein-silver nitrate may prove promising in the food or medical industries.

CONCLUSIONS AND PERSPECTIVES

The constantly expanding field of silver nanocomposites has become of significant importance mainly due to their well proved antimicrobial properties. Synthetic polymers have restricted applications in biomedical fields mainly due to their limited biocompatibility. Silver containing biopolymers have a relatively large potential due to their biocompatibility, low cost and green approach. However, safety concerns have to be considered, since nanosized materials incorporated in either chitosan or soy protein frequently exhibit different properties than those of the corresponding starting materials. Moreover, nanostructures can have more free movement through the body when compared to their higher scale counterparts. Exposure to nanoparticles present in food packaging can occur through dermal contact, inhalation, or ingestion of nanoparticles which have migrated to food.

ACKNOWLEDGEMENTS

The authors wish to thank Environmental Friendly Material Research Society (EFMRS) at BIT Mesra, Patna Campus for motivation while preparing this manuscript.

REFERENCES

1. Fu-Ren F. *et al. Phys. Chem. B* 2002; 106: 279p.
2. Mirsattari S. M. *et al. Neurology* 2004; 62: 1408p.
3. Monafo W. W. *et al. Surg. Clin. North Am.* 1987; 67: 133p.
4. Carsin H. *J. Wound Care* 2004; 13: 145p.

5. Fox C. L. Silver Sulphadiazine, Addendum to Local Therapy. In: *Modern Treatment Hoeber Medical Division*. New York: Harper and Row. 1967. 1259p.
6. Stanford W. *et al. J. Trauma* 1969; 9: 377p.
7. Jones S. A. *et al. Wound Repair Regen.* 2004; 12: 288p.
8. Catauro M. J. *et al. Mater. Sci. Mater. Med.* 2004; 15: 831p.
9. Crabtree J. H. *et al. Perit. Dial Int.* 2003; 23: 368p.
10. Sondi I. *et al. J. Coll. Inter. Sci.* 2004; 275: 177p.
11. Morones J. R. *et al. Nanotechnology* 2005; 16: 2346p.
12. 12 Xu X. H. *et al. Biochemistry* 2004; 43: 10400p.
13. Gogoi S. K. *et al. Langmuir* 2006; 22: 9322p.
14. Elichiguerra J. L. *et al. J. Nanobiotechnol.* 2005; 3: 6p.
15. Kim S. S. *et al. J. Appl. Polym. Sci.* 2011; 119: 2261p.
16. Liu S. *et al. J. Appl. Polym. Sci.* 2013; 129: 3459p.
17. Fernandez A. *et al. Int. J. Food Microbiol.* 2010; 142: 222p.
18. Varma A. J. *et al. Carbohyd. Polym.* 2004; 56: 429p.
19. Murugadoss A. *et al. Nanotechnology* 2008; 19: 015603p.
20. Zhang B. *et al. Int. J. Antimicrob. Agents* 2011; 38: 502p.
21. Creighton J. A. *et al. J. Chem. Soc. Faraday Trans. II* 1979; 75: 790p.
22. Suh J. S. *et al. J. Phys. Chem.* 1983; 87: 1540p.
23. Kim J. S. *et al. Nanomedicine: Nanotechnology, Biology, and Medicine* 2007; 3: 95p.
24. Zhang Y. *et al. Colloids and Surfaces A: Physicochemical and Engineering Aspects* 2013; 423: 63p.
25. Calvo J-J. O. *et al. Environ. Microbiol. Rep.* 2011; 3: 526p.
26. Fikry M. *et al. Carbohyd. Polym.* 2012; 89: 236p.
27. Lu. S. *et al. Burns* 2008; 34: 623p.
28. Liu. B-S. *et al. Macromol. Biosci.* 2008; 8: 932p.
29. Tankhiwale R. *et al. J. Appl. Polym. Sci.* 2010; 115: 1894p.
30. Li G. *et al. J. Appl. Polym. Sci.* 2013; 127: 2690p.
31. Sh S. *et al. J. Food Engg.* 2013; 118: 125p.
32. Sun Q. *et al. J. Food Sci.* 2011; 76: E438p.
33. Zhao S. *et al. Mater. Lett.* 2013; 95: 142p.
34. Zhang Y. *et al. Catal. Comm.* 2013; 34: 35p.

Experimental Analysis of Heat Transfer and Pressure Drop Characteristics of Aluminum Oxide Nanofluid in Tube with Meshes

P. Gopal, M. Chandrasekar*, J. Mohanajaiganesh
Department of Mechanical Engineering, University College of Engineering, BIT Campus, Trichirappalli, Tamil Nadu, India

Abstract

Experimental heat transfer and pressure drop characteristics of Al_2O_3/water nanofluid in a circular tube with meshes and without meshes is reported in this paper. The SEM image of Al_2O_3 nanoparticles in base fluid showed that the particles are uniformly dispersed in base fluid and tiny agglomeration of nanoparticles are present. The experiments were conducted under turbulent conditions with varying flow rates. It is observed the heat transfer rates increased by about 7% and 13% for the case of tube with mesh insert compared to tube without mesh for the water and nanofluid, respectively. At the same time, it is also observed concluded that there is no remarkable increase in friction factor with the use of nanofluids which indicates that the dilute nanofluids having volume concentration about 0.1% can be used for enhancement of heat transfer with no additional pumping power

Keywords: *Nanofluid, heat transfer enhancement, nusselt number, mesh inserts*

****Author for Correspondence*** E-mail: gopal_pp@rediffmail.com

INTRODUCTION

Nanofluids are a relatively new class of fluids which consist of a base fluid with nano-sized particles (1–100 nm) suspended within them. It is introduced at Argonne National Laboratory, USA in 1995. It was found that in both laminar and turbulent flows, convective heat transfer is enhanced in nanofluids as compared with the base fluids. Most studies showed that the heat transfer enhancement increases with increasing nanoparticle concentration and Reynolds number. Moreover, the enhancement generally surpasses what can be expected from the thermal conductivity enhancement alone. Thus, the applicability of the established heat transfer correlations for predicting the thermal transport of nanofluids has been called into question. To further investigate the thermal transport mechanism, a few experimental studies on the pressure drop and convective heat transfer of nanofluids has been reported in the literature. Some selected ones are briefly reviewed in this paper with the emphasis on assessing the applicability of conventional heat transfer correlations for nanofluids and on exploring the heat transfer enhancement mechanisms in nanofluids.

Nanofluids are the next generation heat transfer fluids, and they offer great possibilities of enhanced heat transfer than the ordinary fluids. Even if the use of nanofluids will improve the overall properties and heat transfer characteristics of base fluid and overcome the problems of poor suspension stability and channel clogging of mille and micro particles even then the development and applications of nanofluids may be limited by several factors due to use of very small size solid particles with very small concentration. Chandrasekhar et al. [1] conducted experimental and theoretical investigations of the effective Thermal conductivity and viscosity of Al_2O_3/water nanofluids. The nanoparticles in this study, was prepared using microwave assisted chemical precipitation method and then dispersing them in distilled water using sonicator. During the experimental investigation it was noticed that both the thermal conductivity and viscosity values

increase with that of the nanoparticle volume concentration. Theoretical values obtained were in good agreement with the experimental results. The maximum thermal conductivity obtained was 9.7% for a volume concentration of 3%. Wen and Ding [2] studied the convective heat transfer in the entrance region under laminar regime using aluminium oxide nanofluid in a circular tube with constant heat flux. Migration of nanoparticles and the subsequent disturbance of the boundary layer were attributed to the enhancement in heat transfer rate. Hwang et al. [3] investigated the pressure drop and convective heat transfer coefficient of water based Al_2O_3 nanofluids flowing through a uniformly heated circular tube in fully developed laminar flow regime. The experimental results show that the data for nanofluid friction factor show a good agreement with analytical predictions from the Darcy's equation for single-phase flow. However, the convective heat transfer coefficient of the nanofluids increases by up to 8% at a concentration of 0.3 vol% compared with that of pure water and this enhancement cannot be predicted by the Shah equation. Furthermore, the experimental results show that the convective heat transfer coefficient enhancement exceeds, by a large margin, the thermal conductivity enhancement. In this study, based on scale analysis and numerical solutions, they have shown the flattening of velocity profile induced from large gradients in bulk properties such as nanoparticle concentration, thermal conductivity and viscosity.

Chandrasekar et al. [4] proposed two thermal conductivity models for nanofluid based on the nanolayer thickness and Brownian motion. They reported the nanolayer thickness has no effect on nanofluid thermal conductivity at less than 1% particle volume concentration. Xie et al. [5] measured the thermal conductivity of Al_2O_3/water nanofluid and reported the addition of nanoparticles in base fluid leads to higher thermal conductivity. Syamsunder et al. [6] applied Al_2O_3/water nanofluid in a mini heat exchanger with tube inserts and reported the heat transfer coefficient increases over particle volume concentration. William et al. [7] have studied a variety of nanofluids performance through the horizontal tubes in the turbulent regime. Saqr and Musa et al. [8] investigated the consequence of repetitive fin discontinuity on convective heat transfer coefficient for pipes with internal longitudinal fins and found that smaller the discontinuity offset distance, the higher the convective heat transfer coefficient proved to be. Suresh et al. [9] investigated the heat transfer and pressure drop characteristics through uniformly heated circular tube using Alumina-Copper/water hybrid nanofluids under fully developed laminar flow conditions. In this study, the hybrid particle was synthesized in a thermo chemical route. The volume concentration used was 0.1% and the composition used was 90% Alumina and 10% Copper. The nano composite powder was obtained using hydrogen reduction method and the nanofluids was prepared with the base fluid as water. A maximum enhancement of 13.56% in Nusselt number was obtained for a Reynolds number of 1730 when compared to Nusselt number of water. The friction factor was compared with that of alumina-water nanofluids and was found to be slightly more. Murshed et al. [10] conducted combined experimental and theoretical study on the effective thermal conductivity and viscosity of nanofluids is conducted.

The thermal conductivity and viscosity of nanofluids are measured and found to be substantially higher than the values of the base fluids. Both the thermal conductivity and viscosity of nanofluids increase with the nanoparticle volume fraction. Kim et al. [11] conducted experiments with aluminium oxide and amorphous carbonic nanofluids in the laminar and turbulent regimes and concluded that the mechanism for heat transfer enhancement was different for the two regimes. The delaying and disturbance of the thermal boundary layer was attributed to the heat transfer enhancement in the laminar regime. However, in turbulent regime, increase in thermal conductivity was responsible for heat transfer enhancement. Demir et al. [12] investigated numerically laminar and turbulent forced convection flows of Al_2O_3/water nanofluid as working fluid in a horizontal smooth tube with constant wall temperature and re-ported an enhancement in heat transfer coefficient. Mohammed et al. [13] numerically studied the effects of using nanofluid on the performance of a square shaped micro channel heat exchanger (MCHE). Their results demonstrated that

Al_2O_3 and Ag nanoparticles have the highest heat transfer coefficient and lowest pressure drop among all nanoparticles tested, respectively. They concluded that the benefits of nanofluids such as enhancement in heat transfer coefficient are dominant over the shortcomings such as in-creasing in pressure drop. Similar studies on the potential of nanofluid to act better heat transfer fluid and tube inserts were also reported [14, 15].

Hence in this work, experimental heat transfer and pressure drop characteristics of Al_2O_3/water nanofluid in a circular tube with meshes and without meshes is reported. The behavior of nanofluid in combination with the mesh insert is also explored experimentally. For this purpose, 0.1% vol. Al_2O_3/water nanofluid is formulated without any dispersing agent and the heat transfer and pressure drop studies is performed by circulating the nanofluid in an indigenously fabricated closed loop experimental set up.

PREPARATION OF NANOFLUIDS

Some properties of hydrophilic sphere like Al_2O_3 nanoparticles and base fluid (water) which have been used for assessing the nanofluid properties are tabulated in Table 1. The alumina nanoparticle due to its spherical shape, it has a better heat conduction capability through the fluid.

Table 1: *Thermophysical Properties of Nano Fluid.*

Thermo physical properties	**Al_2O_3 nanoparticles**	**Water**
Specific heat (J/kg/K)	765	4179
Density (kg/m^3)	3800	997.1
Thermal conductivity (W/m/K)	40	0.605
Size (nm)	40–50	-

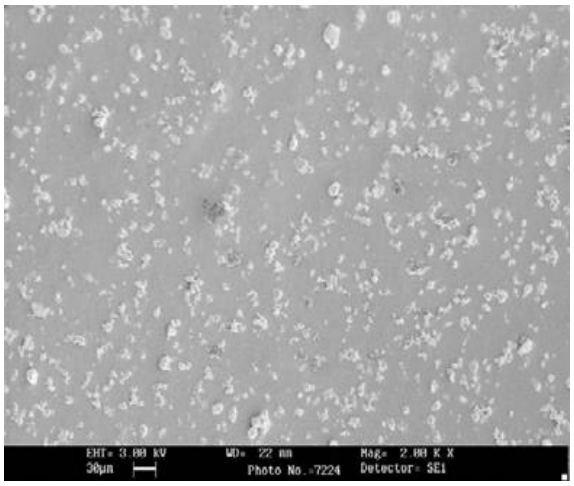

Fig. 1: *SEM Image of Al_2O_3 Nanoparticles.*

Fig. 1 represents the SEM image of Al_2O_3 nanoparticles. The SEM image was obtained by placing the sonicated nanofluid sample on sample holder and then by rapid drying for getting solid particles and finally bringing them conductive. The typical SEM image of Al_2O_3 nanoparticles in base fluid shows that the particles are uniformly dispersed in base fluid and tiny agglomeration of nanoparticles.

EXPERIMENTAL SETUP

The schematic diagram of the experimental setup is shown in Fig. 2. It consists of a calming section, test section, pump, cooling unit, and a fluid reservoir. The test fluid is directed from the reservoir to the calming section and then to the test section using a pump. A valve and a bypass valve are used to control the flow rate. The flow rate is controlled by paddle wheel flow meter. The fluid after passing through the heated section flows through a riser section and then through the cooling unit and finally it is collected in the reservoir. The test section is heated uniformly by the electrical heating wire, attached to an auto-transformer, by which the heat flux can be varied by varying the voltage. Calibrated RTD sensors are used to measure the inlet, outlet and surface temperatures at five different locations.

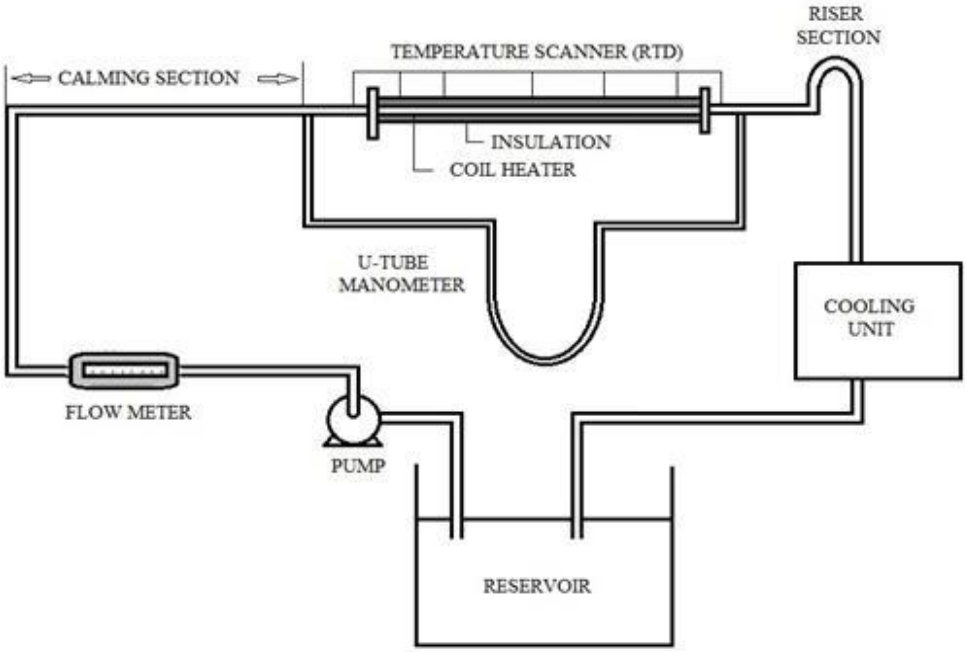

Fig. 2: *Schematic of Experimental Setup.*

The pressure drop across the test section is measured using a U tube manometer with mercury as the manometric fluid. An auto transformer is used to control the surface temperature of heater. A plastic container of 5 liter capacity is used as the fluid reservoir. The test section is wound with ceramic beads coated electrical SWG Nichrome heating wire of resistance 120 Ω. Over the electrical winding a thick insulation is provided using glass wool to minimize heat loss. Thermo wells are mounted on the test section at axial positions in mm of 50, 100, 300, 700 and 950 from the inlet of the test section for installing temperature sensors for outside wall measurements. The photographs of the experimental set up and the mesh insert are shown in Fig. 3.

DATA REDUCTION

The total heat generated by the electrical winding is calculated as,

$$Q_1=VI \quad (1)$$

where, V is the heater input voltage and I is the heater input current. The heat absorbed by the fluid is calculated as,

$$Q_2=mCp\ (T_{out}-T_{in}) \quad (2)$$

where, m is the mass flow rate of fluid, Tin and Tout are the fluid inlet and exit temperatures

$$Q=(Q_1+Q_2)/2 \quad (3)$$

$$q=Q/\pi DL \quad (4)$$

The measured local wall temperature and heat flux are used to calculate the local heat transfer coefficient defined by the following expression:

$$h=q\ /T_w-T_f \quad (5)$$

where, q is the heat flux, T_w is the average wall temperature, and T_f is the average fluid temperature The average Nusselt number is calculated as,

$$Nu=\ h\ D/k \quad (6)$$

where, D is the diameter of the test section, h is the average heat transfer coefficient, and k is the thermal conductivity of the working fluid. The pressure drop (Δp) measured across the test section under isothermal condition is used to determine the friction factor (f) using the following relation:

$$f=\ \Delta pD/0.5\rho v^2L \quad (7)$$

where, v is the fluid velocity, ρ is fluid density, D is the test section diameter and L is the test section length.

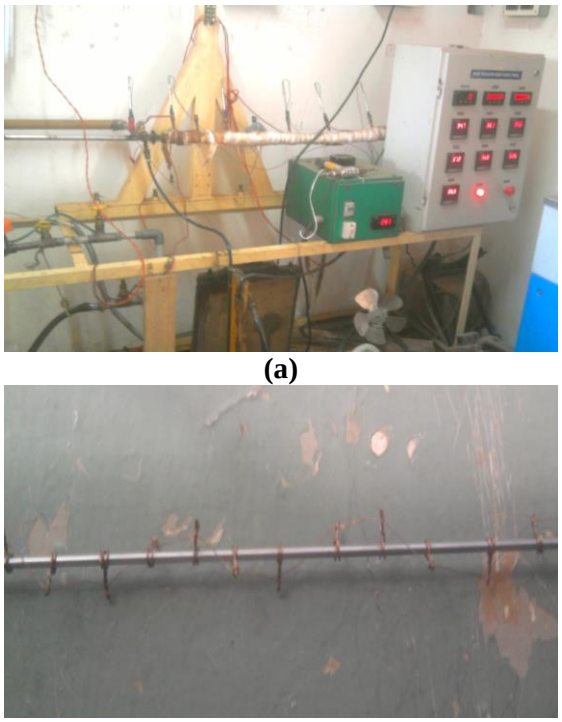

(a)

(b)

Fig. 3: *Photographs of (a) Experimental Setup (b) Mesh Insert.*

Thermo Physical Properties of Nanofluids

The density of Al_2O_3/water nanofluid can be calculated using mass balance as:

$$\rho_{nf} = (1 - \varphi)\,\rho_{bf} + \varphi\rho_{np} \quad (8)$$

where, ρ_{np} and ρ_{bf} are the densities of the nanoparticles and base fluid, respectively, and φ is volume concentration of nanoparticles.

According to the concept of solid-liquid mixture, the specific heat of nanofluids is given by following:

$$Cp_{nf} = (1 - \varphi)\,\rho_{bf}\,cp_{bf} + \varphi\rho_{np}\,cp_{np/}\,\rho_{nf} \quad (9)$$

where, cp_{np} and cp_{bf} are the heat specifics of the nanoparticles and base fluid, respectively. The following curve fitted equation is used for computing the thermal conductivity of nanofluid is expressed in the following form:

$$k_{nf/}\,k_{bf} = 1 + 8.73\,\varphi \quad (10)$$

RESULTS

Heat Transfer Characteristics

The comparison of experimental heat transfer coefficients for water and 0.1% Al_2O_3/water nanofluid are shown in Figs. 4 and 5, respectively.

The increase in heat transfer coefficients are 7% and 13% for the case of tube with mesh insert compared to tube without mesh for the water and nanofluid, respectively. A nearly 100% enhancement is attributed to two factors namely (i) improved heat transfer capability of nanfluid and (ii) the swirl generated by the meah insert in the core fluid flow which in turn catalysis the movement of nanoparicles to better exchange of heat from the tube wall to the fluid core.

Friction Factor Characteristics

The comparison of experimental friction factor for water and 0.1% Al_2O_3/water nanofluid are shown in Figs. 6 and 7, respectively. It is revealed that there is no remarkable increase in friction factor with the use of nanofluids. The friction factor is 0.04742 and 0.0426 for the case of tube with mesh insert for water and nanofluid, respectively. This indicates that the dilute nanofluids having volume concentration about 0.1% can be used for enhancement of heat transfer without much penalty in the pumping power.

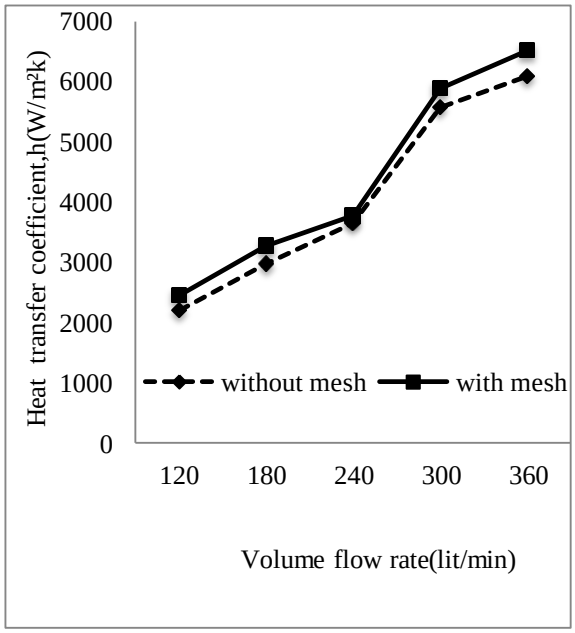

Fig. 4: *Comparison of Heat Transfer Co-Efficient with Mesh and Without Mesh for Water.*

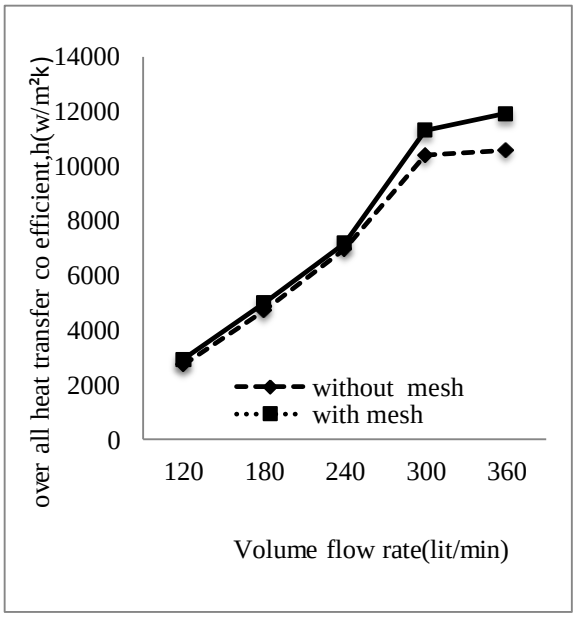

Fig. 5: *Comparison of Heat Transfer Co-Efficient with Mesh and Without Mesh for* Al_2O_3*/water Nanofluid.*

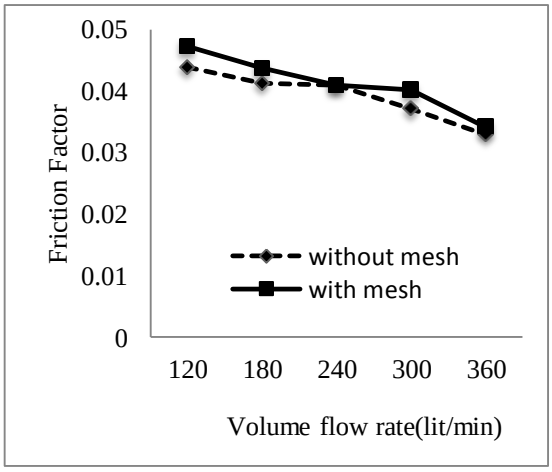

Fig. 6: *Comparison of Friction Factor with Mesh and without Mesh for Water.*

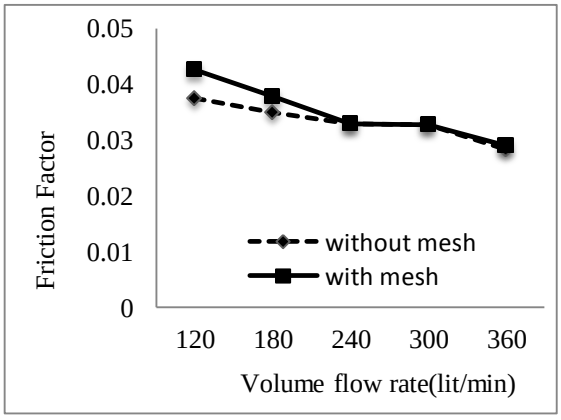

Fig. 7: *Comparison of Friction Factor with Mesh and without Mesh for* Al_2O_3*/water Nanofluid.*

CONCLUSIONS

Experimental heat transfer and friction factor characteristics of Al_2O_3/water nanofluid in a circular tube with meshes and without meshes under turbulent flow conditions was reported. From the experimental results, the following conclusions were drawn:

- The heat transfer rates increased by 7% and 13% for the case of tube with mesh insert compared to tube without mesh for the water and nanofluid, respectively. The enhancement in heat transfer rate is attributed to two factors namely (i) improved heat transfer capability of nanfluid and (ii) the swirl generated by the meah insert in the core fluid flow which in turn catalysis the movement of nanoparicles to better exchange of heat from the tube wall to the fluid core.
- It is also concluded that there is no remarkable increase in friction factor with the use of nanofluids which indicates that the dilute nanofluids having volume concentration about 0.1% can be used for enhancement of heat transfer without sacrificing the pumping power.

REFERENCES

1. Chandrasekar M., Suresh S., Chandra Bose A., Experimental Investigations and Theoretical Determination of Thermalconductivity and Viscosity of Al2O3/water Nanofluids. *J. Exp. Therm. Fluid Sci.* 2010; 34: 210–216p.
2. Wen D., Ding Y., Formulation of Nanofluids for Natural Convective Heat Transfer Applications. *Int. J. Heat and Fluid Flow*.2005; 26: 855–864p.
3. Hwang K.S., Jang S.P., Choi S.U.S., Flow, Convective Heat Transfer Characteristics of Water-based Al2O3 Nanofluids in Fully Developed Laminar Flow Regime. *Int. J. Heat Mass Trans*.2009; 52: 193–199p.
4. Chandrasekar M., Suresh S., Srinivasan R., New Analytical Models to Investigate Thermal Conductivity of Nanofluids. *J. Nano Sci. Nano Tech*.2009; 9: 533–538p.
5. Xie H., Wang J., Xi T., *et al.* Thermal Conductivity Enhancement of Suspensions Containing Nanosized Alumina Particles. *J. Appl. Phy*. 2002; 91: 4568–4572p.
6. Syamsunder S., Sharma K. V., Ramanathan S., Experimental Investigation of Heat Transfer

Enhancement with Al2O3 and Twisted Tape Insert in a Circular Tube. *Int. J. Nanotech. Appl*. 2007; 2: 21–28p.

7. Williams W., Buongiorno J., Hu L.W., Experimental Investigation of Turbulent Convective Heat Transfer and Pressure Loss of Alumina/water and Zirconia/water Nanoparticle Colloids (nanofluid) in Horizontal Tubes. *J. Heat Trans.* 2008; 130: 042412 – 042417p.
8. Saqr K.M., Musa M.N., Numerical Study of the Heat Transfer Augmentation in Pipes with Internal Discontinues longitudinal Fins. *Int. J. Mech. Mater. Eng.* 2009; 4: 62–69p.
9. Suresh S., Venkitaraj K.P., Selvakumar P., *et al.* Effect of Al2O3–Cu/water Hybrid Nanofluid in Heat Transfer. *J. Exp. Therm. Fluid Sci.* 2012; 38: 54–60p.
10. Murshed S.M.S, Leong K.C., Yang C., Thermophysical and Electrokinectic Properties of Nanofluids – A Critical Review. *Appl. Therm. Eng.* 2008; 28: 2109–2125p.
11. Kim J., Kang Y.T., Choi C.K., Analysis of Convective Instability and Heat Transfer Characteristics of Nanofluids. *Phys. Fluids.* 2006; 16: 2395–2401p.
12. Demir H., Dalkilic A.S., Kurekci N.A., *et al.* A Numerical Investigation of Nanofluids Forced Convection Flow in a Horizontal Smooth Tube. *Int. Heat Transfer Conference*.2010; ASME, USA.
13. Mohammed H.A., Bhaskaran G., Shuaib N.H., *et al.* Influence of Nanofluids on Parallel Flow Square Micro Channel Heat Exchanger Performance. *Int. Commun. Heat Mass* 2011; 38: 1–9p.
14. Rea. U, Laminar Convective Heat Transfer and Viscous Pressure Loss of Alumina-Water Nanofluids. *Int. J. Heat Mass Tran.* 2009; 52: 2042–2048p.
15. Sivashanmugam P., Suresh S., Experimental Studies on Heat Transfer and Friction Factor Characteristics of Laminar Flow through a Circular Tube Fitted with Regularly Spaced Helical Screw-Tape Inserts. *Exp. Therm. Fluid Sci*.2007; 31: 301–308p.

Fundamentals of Picoscience

Edited by: Klaus D. Sattler
Published by: CRC Press, Taylor & Francis Group, Boca Raton, FL., USA
Contents: 756 Pages; 769 Illustrations; Price: 179.95 USD, Hardback
ISBN: 13:978-1-465-0509-4
Reviewed by: Hardev S. Virk

The book under review consists of 37 Chapters which are further divided into IX parts, namely, Picoscale Detection, Picoscale Characterization, Picoscale Imaging, Scanning Probe Microscopy, Electron Orbitals, Atomic Scale Magnetism, Picowires, Picometer Positioning, and Picoscale Devices. As the Section headings suggest, the Book proposes to cover the methods and materials at the picometer-size scale, which is the next size range, three orders of magnitude, below nanometer.

Nanoscience has brought many new effects and inventions and is the basis for worldwide surge in nanotechnology. Currently, there are more than one million scientists involved in projects with nanoscale structures and materials. From the development of new quantum mechanical methods to far reaching applications in electronic industry and medical diagnostics, nanoscience has inspired numerous scientists and engineers to new instrumental developments and inventions. "Nano" has become the buzz word for extremely small even for the general public and many surprises can be expected in the future for structures at nanoscale.

We are entering an era of ever smaller and more efficient devices, which will rely on smaller designs and structures three orders below the nanometer scale. Do we already have instruments to probe below the nano-range? How can we develop new instruments to visualize and measure structures at the subnnometer size? Answers to these and other questions are given in this book, Fundamentals of Picoscience.

One picometer is the length of a trillionth of a meter. Compared to a human cell of typically ten microns, this is roughly ten million times smaller. In this state-of-the-art book, international scientists and researchers at the forefront of the field present the materials and methods used at the picoscale. They address the key challenges in developing new instrumentation and techniques to visualize and measure structures at this sub-nanometer level. The main purpose of this book is to help the young researchers to understand the implications of picoscience, e.g., to understand how picoscience is an extension of nanoscience; to determine which experimental technique to use in your research, and to connect basic studies to the development of next-generation picoelectronic devices.

The book under review covers various approaches for detecting, characterizing, and imaging at the picoscale. It then presents picoscale methods ranging from scanning tunneling microscopy (STM) to spectroscopic approaches at sub-nanometer spatial and energy resolutions. It also covers novel picoscale structures and picometer positioning systems. The book concludes with picoscale device applications, including single molecule electronics and optical computers. The learned authors of each chapter of this book explain basic concepts, define technical terms, discuss theoretical background and give illustrations in reference to the context to explain the main purpose of their chapter.

Chapter 20, authored by David M. Villeneuve, refers to "Attosecond Imaging of Molecular Orbitals". The author makes use of High Harmonic Spectroscopy to probe the position of atoms within the molecule. This is where the new field of attosecond science shows much promise. An attosecond is an SI unit of time equal to 10^{-18} of a second (one

quintillionth of a second). Lasers can now generate light pulses down to 100 attoseconds thereby enabling real-time measurements on ultra-short time scales that are inaccessible by any other methods.

It is not possible to review contents of all 37 Chapters of this book. The underlying principle of most of these Chapters is the role played by the measurement techniques in the study of picoscale structures. In fact these very techniques are used to explore matter at the nanoscale also. The invention of Scanning Tunneling Microscope (STM) has brought a revolution in measurement techniques. When STM was invented, the main feature was to observe atomic configurations of surface atoms in real space. In Chapter 22, the authors have illustrated how to study atomic-scale magnetism by Spin-Polarized Scanning Tunneling Microscopy (SP-STM). The understanding of magnetism at the ultimate atomic length scale is one of the current frontiers in solid state physics, which is the main purpose of this Chapter.

The last six Chapters of the book deserve special attention of the readers. These deal with Picoscale Devices: Mirrors with sub-nanometer surface shape accuracy; Single Molecule Electronics; Single-atom Transistors for Light; Carbon-based zero-, one-, and two-dimensional materials for Device Application; Subnanometer Characterization of Nanoelectronic Devices; and Chromophores for Picoscale Optical Computers.

The salient features of this book are enumerated as follows:

- Details all experimental techniques for picoscale studies, including atomic-scale optical and neutron holography, homodyne and heterodyne interferometry, digital holographic microscopy, single-atom STM, orbital-mediated tunneling spectroscopy (OMTS), electron energy loss spectroscopy (EELS), transmission electron microscopy (TEM), and x-ray absorption fine structure (XAFS);
- Explains how to determine the atomic structure of proteins and individual peptides through electron diffractive imaging and coherent x-ray diffraction imaging;
- Explores the future of picoelectronic devices, such as molecular electronic applications, NEM single-atom switches, a picomotor, single-photon quantum devices, and single-photon gating systems;
- Includes introductions that explain basic concepts, defines technical terms, and gives theoretical approach to the basic phenomenon under discussion.

The Editor has done excellent job in selection of Section themes and organising the Chapters in an appropriate manner. The literature survey is very exhaustive and effort has been made to list references in full measure, giving titles of papers with page numbers and even month of publication where ever possible. There are hardly any typo mistakes that came to my notice. I hope the research community will welcome this book, claimed by the publishers as the first of its kind at global level, on Fundamentals of Picoscience.

Hardev S. Virk
Visiting Professor
SGGS World University, Fatehgarh Sahib
Guest Editor
Trans Tech Publications (Switzerland)

A Nanotechnology platform

Nano Science and Technology Consortium
(A division of Consortium e-Learning Network Pvt. Ltd.)

HURRY! ADMISSION OPEN!

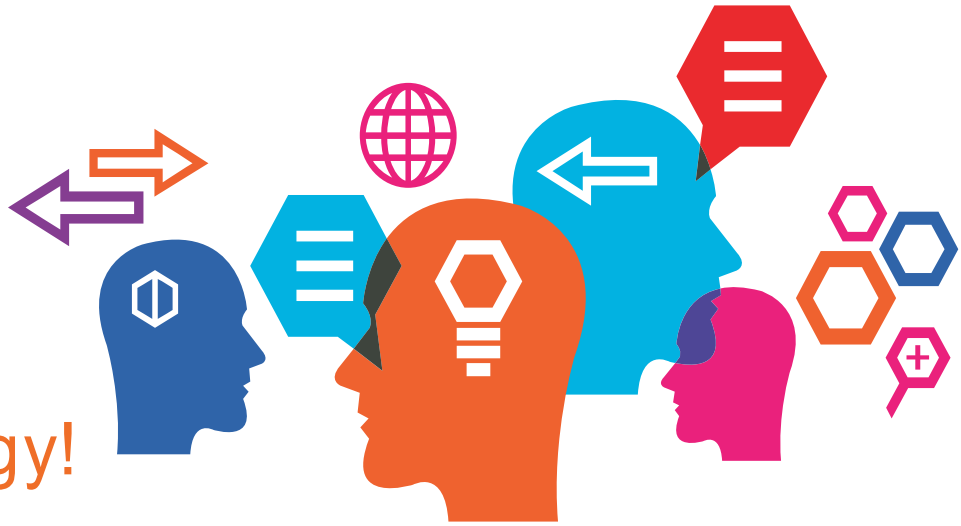

Learn Nanotechnology! Stay Ahead!

Nanotechnology is the emerging field in Science & Technology and is poised to bring in revolutionary changes across all spheres of life.

NSTC is India's leading institute for certificate training in Nanoscience & Nanotechnology. Our training portfolio includes courses suitable for students from most Scientific and Engineering backgrounds, and tailored to the main areas of research and development in nanotechnology.

Program Highlights

* Smart e-Learning Module
* Learn at your own pace, on your schedule (24 ×7 access), from any location with internet access
* Online guidance and tutoring
* User friendly teaching environment
* Course content designed by highly competitive faculty from various reputed institutes like IIT, BHU, NITs etc.
* Greater choices of Projects, catering to Research as well as Business aspect of Nanotechnology
* Online Exams
* Regular progress tracking
* Evaluation and Certification

Nanotechnology eLearning Programs

* Nano Sensitization Program
* Introductory Program in Nanotechnology
* Integrated Program in Nanotechnology
* Industry Program in Nanotechnology
* Nano Electronics & Industrial Applications
* Nanopharmaceuticals & Its Industrial Applications
* Bionanotechnology & its Industrial Applications
* Nanotechnology Teacher's Training Program
* Summer/Winter Project Work

Advanced Teaching Methodology
Study Material (Printed) +Web-based learning

Program duration
3 to 9 months

Avail Scholarship!
For meritorious students and group joiners.

Contact NSTC for more details!

A-118, First Floor, Sector-63, Noida-201301 | P: +91 120 4781 215, (M): 9958161117
www.nstc.in | info@nstc.in

eLearning | Journals | Technology Transfer | Consulting | Outsourcing